Quantum Fluctuations in a Segmented Ionization Chamber for Beam Monitoring of Synchrotron Radiation

THESIS
for obtaining the Degree of Doctor
of Natural Sciences

Presented by
Syed Naeem Ahmed
from Karachi

Submitted to Physics Department
of Siegen University
Siegen 1998

Table of Contents

1. Introduction

During the last two decades, the immense use of synchrotron radiation in different fields of science and technology has made the development of more and more precise detection systems a necessity. The range of applications of these new bright light sources are diverse and so are the respective detection systems.

In some of the experiments with synchrotron radiation it is desirable that the intensity of the incoming beam be precisely measured before the actual experiment is performed. One of such experiments concerns the extraction of detailed structure of different materials from Extended X-ray Absorption Fine Structures (EXAFS). The detailed discussion on these experiments can be found elsewhere (see, for example, [Margaritondo, 1988]). The majority of these experiments are performed in transmission mode, in which the beam is passed through the sample and the incoming and outgoing intensity (I_0 and I respectively) is measured (see fig.1.1)

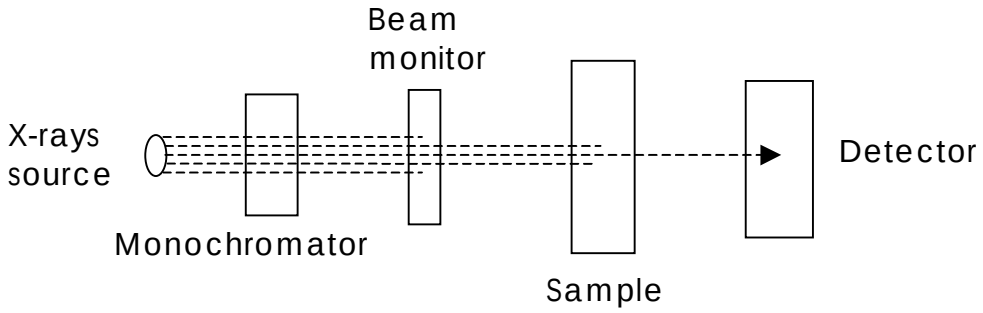

Fig.1.1. Sketch of principle of EXAFS experiment performed in transmission mode.

The absorption coefficient μ of the sample of thickness x can then be measured by taking logarithm of ratio of these two intensities [Margaritondo, 1988],

$$\mu = -\frac{1}{x}\ln\left(\frac{I}{I_0}\right)$$

This absorption coefficient measured as a function of photon energy gives information about the structure of the sample. It is apparent that the linearity and noise of both the detectors are very crucial in extracting useful information from the measurements. The detector in front of the sample has the additional constraint that it should not absorb an appreciable portion of the beam because in that case not enough photons will be available to be effectively transmitted and detected by the spectrometer behind the sample. However these beam monitors also need to absorb at least a certain number of photons to achieve desired precision. Exploiting the Poisson nature of the absorption process one can get at least an order of magnitude estimate of the minimum number of photons which must be absorbed to achieve certain precision. For example, for a precision of better than 10^{-4}, more than 10^8 photons must be absorbed ($\{\sigma_N/N\}=\{N^{1/2}/N\}<10^{-4} \Rightarrow N>10^8$). These two contradictory requirements make the design of such systems difficult. During this work such a beam monitor has been developed and tested with a powerful X-ray tube.

1.1. Choice of Detector

The beam monitor constructed here has been designed to work in the energy range from 5keV to 20keV of incident photon. At lower energy range around 5keV, the high absorption of incident photons in solids immediately forbid their use as conversion materials. In this case the use of a gaseous detector is favored. The gaseous detectors can be either quantum detectors or integrating devices. It is known that at higher rates, the integrating systems show better performance for intensity measurements as compared to single photon counting systems. This can be understood by the following argument.

The detective quantum efficiency of an integrating detector with absorption efficiency QE is given by (see section 3.1),

$$(DQE)_{int} = \frac{QE}{1+\frac{\sigma_{add}^2}{QE \cdot N_{in}}} \qquad (1.1\text{-}2)$$

while that of a quantum detector with a paralysable dead time τ and measurement time Δt it is [Walenta 1994],

$$(DQE)_{quant} = QE \cdot \left(1-\frac{QE \cdot \tau \cdot N_{in}}{\Delta t}\right)^2 \cdot exp\left(-\frac{QE \cdot \tau \cdot N_{in}}{\Delta t}\right) \qquad (1.1\text{-}3)$$

The exponentially decreasing behavior of detective quantum efficiency of quantum detectors with increasing incident number of photons limits its usefulness at higher incident fluxes. On the other hand the increasing DQE of integrating systems with increasing incident photon numbers reaching the limiting value of absorption efficiency favors their use as intensity monitors for synchrotron radiation. Fig.1.1.1. shows the plot of equations 1.1-2 and 1.1-3 with respect to incident number of photons for an absorption efficiency of 10%.

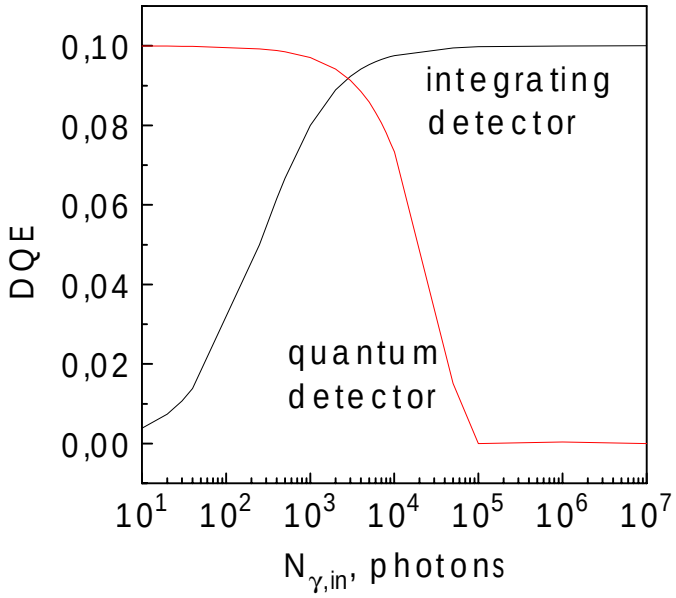

Fig.1.1.1. DQE of integrating and quantum detectors.

It can be seen that the detective quantum efficiency of an integrating detector increases rapidly with respect to incident number of photons and

quickly reaches the limiting value of absorption efficiency. On the other hand, the DQE of a quantum detector falls off quickly and makes its use impractical at high incident photon rates.

Since the typical photon intensity from a synchrotron radiation source is of the order of 10^{10} per second, therefore the single photon counting systems (quantum detectors) can not be employed as beam intensity monitors. This led to the development of a segmented ionization chamber as the beam intensity monitor. In the following we review some of the basic features of such a system.

1.1.1. Selected Mode of Operation

In current mode operation, the instantaneous current can be measured by some device connected to the readout electrode. Such a method is highly susceptible to different sources of noise specially when the ionization current is very low (less than a pico ampere) and hence very sophisticated and expensive instruments are needed to minimize measurement uncertainties. Alternatively, the corresponding charge can be integrated for a certain time on a capacitor and the resulting voltage can be recorded. This method has two clear advantages over the former one. Firstly, because the signal is amplified therefore more inherent noise of the system is affordable. Secondly, in this case the system is more flexible in the sense that the integration time and the integration capacitance can be varied according to the application and the acceptable noise.

The Ramo's theorem [Delaney 1984] can be used to find the instantaneous current in an ionization chamber. It states that the instantaneous current i received by an electrode due to the motion of a charge q with velocity v is given by $i=E_v qv$, where E_v is the component in the direction v of that electric field which would exist at the charge's instantaneous position under the following circumstances: charge removed, given electrode raised to unit

potential, all other conductors grounded. According to this definition, for a parallel plate chamber the electric weighting field $E_v=1/d$, d being the electrode separation, and the current is given by,

$$i = \frac{q \cdot v}{d}$$

The usual method is to collect the corresponding charge on an external capacitor for a certain time and to measure the resulting voltage. This is accomplished by an integrator connected directly to the readout electrode, as shown in fig. 1.1.1-1.

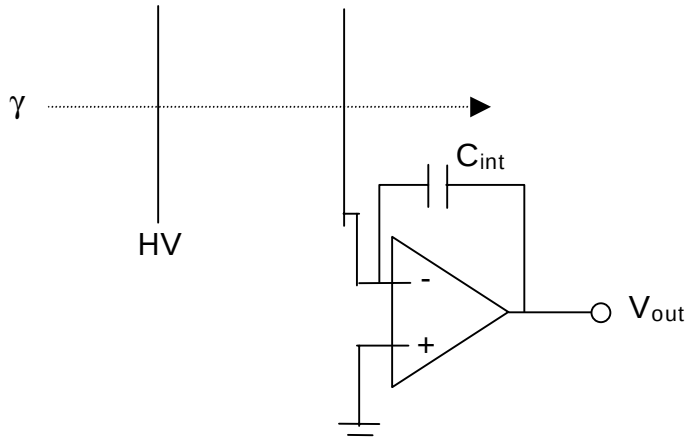

Fig.1.1.1-1. Schematic of beam monitor's operation principle.

The corresponding voltage change rate at the output of the integrator should be linearly dependent on the input current and should be derivable from the transfer function of the integrator. For a perfect integrating circuit, the output should be,

$$V_{out} = \frac{1}{C}\int_0^{\tau} i \cdot dt \qquad (1.1.1\text{-}1)$$

Where C is the integration capacitance and τ is the integration time. If the input current is constant during the integration time then the above relation reduces to,

$$V_{out} = \frac{i \cdot \tau}{C} \qquad (1.1.1\text{-}2)$$

As mentioned before, this method has the advantage over direct current measurement because the output voltage is amplified and can be more easily measured. Furthermore, its value can be controlled by changing integration time and capacitance according to the requirements of the particular application.

1.1.2. Intensity Measurement and Corresponding Fluctuations

If dN_{abs}/dE represents the un-normalized spectrum of photons *absorbed* during integration time then the measured intensity is given by,

$$I = \int_{E_{min}}^{E_{max}} E \cdot \frac{dN_{abs}}{dE} \cdot dE \qquad (1.1.2\text{-}1)$$

For a detector having absorption efficiency QE, this can be written in terms of un-normalized spectrum of incident photons dN_{in}/dE, i.e.,

$$I = \int_{E_{min}}^{E_{max}} QE \cdot E \cdot \frac{dN_{in}}{dE} \cdot dE \qquad (1.1.2\text{-}2)$$

This shows that the measured intensity is proportional to the total deposited energy.

The corresponding Poisson fluctuations in the measured intensity is given by (see section 4.4.2),

$$\sigma^2 = < E_\gamma >^2 \cdot N_{abs} \cdot \left[1 + \frac{\sigma_E^2}{< E_\gamma >^2} \right] \qquad (1.1.2\text{-}3)$$

Here σ_E is the spread in the spectrum of *absorbed* photons.

However, this is not the only noise in the measured intensity. The additional noise sources include electronics noise and contamination in the detector. In chapter 5 some of the dominant noise sources have been discussed in detail.

The inclusion of additional noise term in the above relation gives the amount of total fluctuations in the measured data, i.e.,

$$\sigma_{total}^2 = \sigma_{add}^2 + < E_\gamma >^2 \cdot N_{abs} \cdot \left[1 + \frac{\sigma_E^2}{< E_\gamma >^2} \right] \qquad (1.1.2\text{-}4)$$

The above relation shows that the precision of the intensity measurement also depends weakly on the spread in the spectrum of absorbed photons. And since the spectrum of absorbed photons depends on the spectrum of incident photons, therefore, the more monochromatic the incident beam is, the better is the precision of measurement, provided all other parameters are kept constant.

2. Consideration of Physical Processes for Design Optimization

While designing the beam monitor with given constraints, it is necessary to optimize the design parameters taking into account the physical processes inside the chamber. These physical processes give an idea of the physical limits of the system. In this chapter we will look into some of these processes and how they were used for designing the chamber.

The photons passing through the filling gas of the chamber produce electron ion pairs. This is a complex quantum mechanical phenomenon and can not be analytically solved for a general geometry. Fortunately, the Poisson nature of the process makes it easy to estimate the fluctuations in the number of charge pairs produced. The applied electric field between the electrodes forces the electrons and ions to move in opposite directions. The important aspects of the generation of electron ion pairs and their movement resulting in development of electrical signal at the readout electrode are discussed below.

2.1. Interaction of Photons

Photons interact with matter in fundamentally two different ways: they are either absorbed or scattered through a certain angle. The absorption can be either photoelectric absorption or the one which initiates pair production. In Compton effect the photons are scattered either by quasi-free electrons or by the target nucleus. All these processes are statistical in nature and are represented by their respective interaction probabilities (cross sections). These cross sections depend both on the energy of the incoming photons and the target material. Fig.2.1-1. shows the ranges in which the above mentioned three processes dominate as a function of the photon energy and the target charge. It can be seen that in the energy range of our interest (5keV to

20keV), the photoelectric effect dominates for the filling gas argon. Therefore in the following we will discuss only the photoelectric effect.

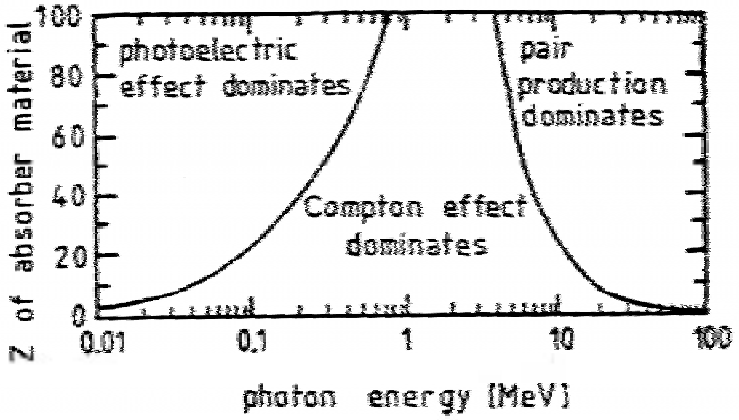

Fig.2.1-1. The range of domination of the three basic physical processes of photon interaction [Grupen 1996]

2.1.1. Photoelectric Effect

The photoelectric effect is characterized by the absorption of a photon by an atomic electron with the subsequent ejection of the electron from the atom. This process can not occur for free electrons because in that case the momentum will not be conserved. The proximity of atomic nucleus allows the recoil momentum to be transferred to the nucleus. The energy of the ejected photoelectron is given by,

$$E = h\nu - B.E.$$

Where B.E. is the binding energy of the electron and ν is the frequency of the incoming photon.

Fig.2.1.1-1 shows a typical photoelectric absorption cross section behavior as a function of incident photon energy. It can be seen that at energies above the K-shell energy, the cross section is relatively small but increases very rapidly as the K-shell energy is approached. After this point the K-shell electrons, because of their higher energy, are no longer available for

photoelectric interaction and consequently the cross section drops drastically. This sudden dip is known as the K-edge of the particular material. At lower energies the L-, M-edges etc. are found. However if the incident photon energy is larger than the K-shell binding energy, then roughly 80% of the interactions occur between incident photons and the K-shell electrons. This can be explained by the proximity of the atomic nucleus to the K-shell which can take the recoil momentum.

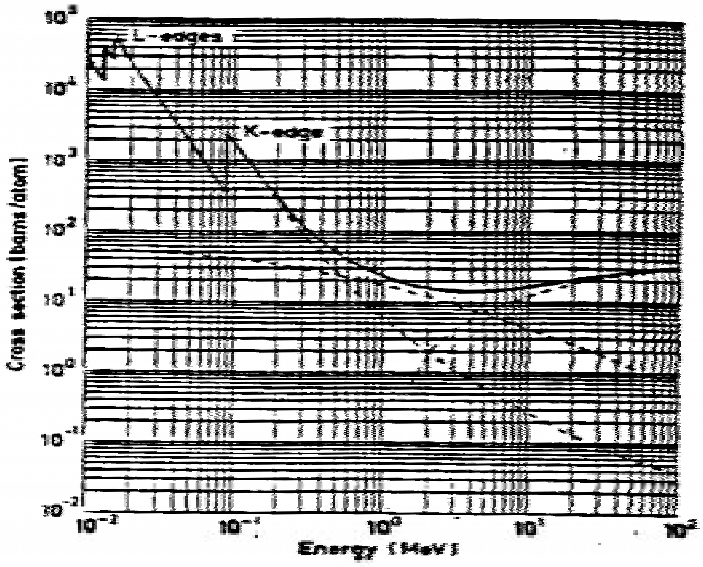

Fig.2.1.1-1. Photoelectric absorption cross section of lead [Leo 1994]

In our case where the incident photon energy is not very large (5-20 keV), the total photoelectric cross section away from the absorption edges can be calculated using Born approximation [Leo 1994, Grupen 1996],

$$\sigma_{photo} = 4\alpha^4 \sqrt{2} Z^5 \sigma_{Th}^e \left(\frac{m_e c^2}{E_\gamma} \right)^{7/2} \qquad cm^2/atom$$

Where $\sigma_{Th}^e = 8\pi r_e^2 / 3 = 6.651 \times 10^{-25} \quad cm^2$ is the Thompson cross section, and $\alpha = 1/137$.

For energies closer to the K_edge, this must be multiplied by a correction factor to give [Leo 1994],

$$\sigma_{photo}^{K} = \sigma_{Th}^{e} \frac{2^2 \pi (137)^3}{Z^2} \left[\frac{\nu_K}{\nu}\right]^4 \frac{\exp\left(-4\xi \cot^{-1}\xi\right)}{1-\exp(-2\pi\xi)} \quad cm^2 / atom$$

Where $h\nu_K = (Z-0.03)^2 m_e c^2 \alpha^2 / 2$ and $\xi = \sqrt{\nu_K / (\nu - \nu_K)}$

Some secondary effects may also occur as a result of the photoelectric effect in an inner shell. If the free space is filled by an electron from a higher shell, the energy differences between these two shells may be liberated in the form of characteristic X-rays. This energy may also be transferred to an electron of the same atom. If this energy is larger than the binding energy of the electron in that particular shell then the electron can leave the atom. This effect is known as Auger effect and the liberated electron is called Auger electron. The energy of these Auger electrons is small as compared to the energy of the primary photoelectrons.

2.1.2. Total Photon Absorption Cross-Section

There is always some probability that the incoming photons may interact with target molecules by reactions other than photoelectric effect, for example, Compton scattering. Therefore while calculating the total absorption and number of total electron ion pairs generated, it is necessary to use the total absorption cross section. The total probability for a photon interaction is generally written as the sum of the individual cross sections of photoelectric effect, Compton scattering and pair production, i.e.,

$$\sigma_{total} = \sigma_{photo} + Z\sigma_c + \tau_{pair} \qquad (2.1.2\text{-}1)$$

The other reactions of photons such as photonuclear reaction, photon-photon scattering, etc. have extremely low cross sections [Grupen 1996] and therefore have essentially no importance for the detection of photons. Furthermore the minimum energy required for pair production is very large

(511keV) as compared to our energy range of interest (<20keV) and therefore this effect can also be ignored for the present case.

Since only part of photon energy is transferred during Compton scattering, therefore it is almost always necessary to use total attenuation coefficients rather than total absorption coefficients. The total mass attenuation coefficient is calculated by multiplying equation (2.1.2-1) by the density of atoms (or molecules) in the target material. The attenuation of photons of intensity I_0 travelling a distance x of material with total mass attenuation coefficient μ then follows according to the exponential law,

$$I = I_0 \exp(-\mu x)$$

Fig.2.1.2-1 shows the energy dependence of mass attenuation coefficient and mass absorption coefficient for photons in air. It should be noted that the difference between the two almost vanishes at energies below 20keV, thus emphasizing that at such energies the dominant mode of interaction is photoelectric effect.

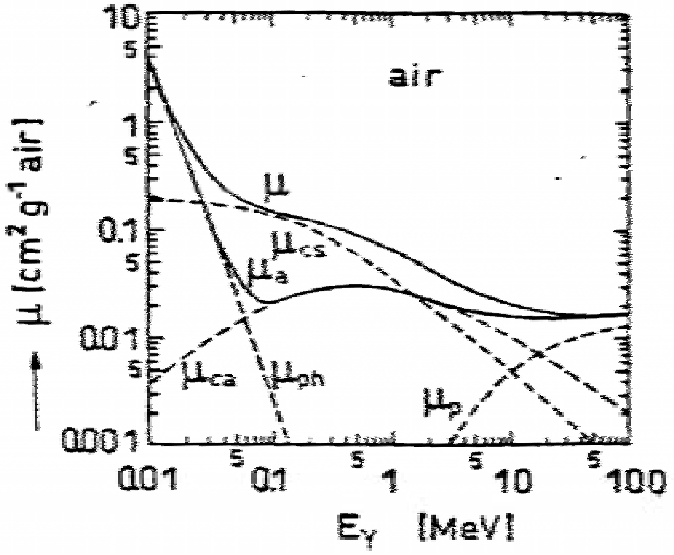

Fig.2.1.2-1. Energy dependence of attenuation coefficients for photon in air [Grupen 1996]

2.1.3. Production of Electron-Ion Pairs

Both absorption and scattering of photons are statistical processes and one can only talk about the respective probabilities of occurrence. Consequently the production of electron ion pairs is also statistical in nature. Fortunately the mean energy needed to produce an electron ion pair depends very weakly on type of incident particle and its energy. Therefore one can estimate the mean number of charge pairs produced by the passage of photons of energy E_γ through a thickness x of material having mass attenuation coefficient μ by,

$$N_{e-ion} = \frac{N_O E_\gamma \left(1 - e^{-\mu x}\right)}{W}$$

Here W represents the energy needed to produce an electron ion pair.

The W-value is weakly dependent on the type of gas. Table 2.1.3-1 gives measured values of some commonly used gases in radiation detectors.

Table 2.1.3-1. W-values for various gases [Leo 1994]

Gas	W-value, eV
Ar	26
Kr	24
Xe	22
CO_2	33
CH_4	28

2.2. Optimization of Design Parameters

Different design criteria were taken into account to make the system a practical beam intensity monitor of x-ray beams. The main focus of these criteria was on the use of the monitor in EXAFS experiments. However, the

system is in no way specific for such experiments and can be used wherever high precision beam intensity monitoring of synchrotron radiation is required. The main design criteria were:

- The system should be able to work at rates as high as 10^{12} photons/mm^2 s.
- It should work in the energy range of 5-20keV.
- It should not attenuate the original photon beam to an unacceptable level: ~5% at higher energies and ~20% at lower energies.
- The precision of intensity measurement should be better than 10^{-4}.
- Largest incident photon beam area: 4X10 mm^2.

The number of electron-ion pairs produced in the chamber per unit time is a function of the amount of gas in the active volume of the chamber. The active length is therefore a critical parameter which should be optimized according to the given constraints. The precision requirement sets the most fundamental limit on the minimum active length of the chamber. For getting the precision of at least 10^{-4} one can find the threshold value of active length below which such a precision is impossible to achieve. The Poisson nature of the photon absorption process implies that the variance in the number of absorbed photons is equal to its square root for a mono-energetic photon beam, i.e.,

$$\sigma_{abs} = \sqrt{N_{abs}}$$

For a system which behaves linearly with respect to number of absorbed photons, the precision in measurement is equal to the relative quantum fluctuation in the number of absorbed photons. Here we have neglected electronics noise and digitization error because they are insignificantly small as compared to the Poisson fluctuations at high photon rates (compare typical total electronics noise of 200 equivalent absorbed photons to the Poisson noise of 10^5 for 10^{10} absorbed photons). For our case, this precision in measurement should be better than 10^{-4},

$$\frac{\Delta I_{ion}}{I_{ion}} = \frac{\sigma_{abs}}{N_{abs}} = \frac{1}{\sqrt{N_{abs}}} \leq 10^{-4}$$

Here I_{ion} represents the measured ionization current.

This gives the physical limit on the minimum number of photons which must be absorbed to obtain the required precision,

$$N_{abs} \geq 10^{8} \qquad (2.2\text{-}1)$$

The number of photons being absorbed per unit time in a simple parallel plate ionization chamber is given by,

$$N_{abs} = N_{in}(1 - e^{-\mu x}) \qquad (2.2\text{-}2)$$

Where N_{in} is the incident number of photons per unit time, μ is the mass attenuation coefficient of the filling gas and x is the length of the active volume.

Equation (2.2-2) together with condition (2.2-1) gives the physical limit on the minimum length of the active volume,

$$x \geq -\frac{1}{\mu} \ln\left(1 - \frac{10^{8}}{N_{in}}\right) \qquad (2.2\text{-}3)$$

Since the mass attenuation coefficient is dependent on photon energy, therefore the minimum active length depends not only on the number of incident photons but also on their energy. Fig.2.2-1 shows a plot of threshold active length as a function of photon energy for two different filling gases and different numbers of incident photons. It is evident from the plot that the active length threshold increases with increase in percentage of admixture (methane) in the filling gas. Since the main purpose of this admixture is to decrease the absorption therefore it is desirable to keep the length as large as possible so that the required precision remains achievable. For a mixture of

90% argon and 10% methane at normal pressure the active length should not be less than about 12mm. At this value the absorption in the gas is roughly 7%.

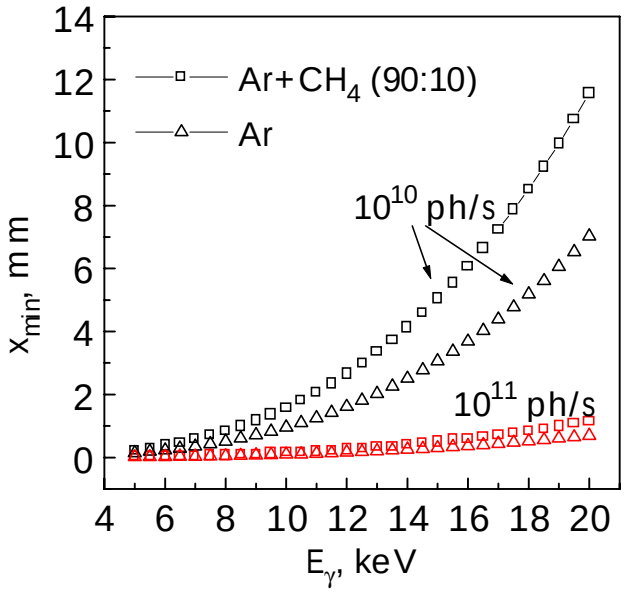

Fig.2.2-1. Energy dependence of active length threshold.

Once the active length has been fixed, the absorption in the chamber can be controlled by changing the concentration of admixture in the filling gas or even by using some other gas. Therefore it is not necessary to optimize the system with respect to absorption.

The electrons and ions generated by the passage of x-ray beam through the active volume of the chamber move in opposite directions under the influence of applied electric field. Because of the relatively slower movement of ions, they tend to accumulate on one side of the chamber. This space charge changes the electric field inside the active volume and consequently the movement of electrons (and ions) is disturbed. A detailed calculation of space charge effect in the constructed beam monitor can be found in Appendix-A. Appendix-B contains a brief discussion and numerical data concerning the motion of electrons and ions in the chamber.

The space charge effect becomes significant at high photon rates (>10^{11} photons/s) (see fig.A-2) and disturbs the applied electric field such that it no

longer remains uniform throughout the active length. This, of course, affects the drift of electrons (their drift velocity depends on electric field, see Appendix-B) and ions. Also the recombination losses might increase in region of low electric field. The system will therefore behave no more linear with respect to incident number of photons. There are two solutions to this problem. Firstly one can apply high enough electric field such that even at high photon rates the space charge does not lower the electric field to allow increase in recombination rate. Secondly the active length can be kept small such that the electrons and ions have to move very small distances before being collected by the electrodes and consequently the effect becomes insignificant. Since there are other constraints on the maximum electric field which could be applied (to avoid gas breakdown and discharge) and the minimum length which could be kept (active length threshold) therefore the best solution is to apply both of these methods simultaneously.

As mentioned earlier, it is not possible to decrease the length below a certain threshold (e.g. 12mm for a mixture of 90% argon and 10% methane at normal pressure). The solution to this problem is to make more active regions instead of one. Keeping this in view, the beam monitor was designed with two 8mm thick active regions giving a total of 16mm active length. The other advantage of having two regions is that the charge-collection efficiency increases (because of two electrodes for collection of each type of charge).

The detailed design of the system is described in the next chapter.

3. Design and Construction of the Beam Monitor

The constructed beam monitor is a segmented parallel plate ionization chamber. In the following a brief description of chamber design and construction is presented.

3.1. Design Criteria

The design criteria of the beam monitor were mentioned in the last chapter. Based on the constrains of measurement precision and physical processes, the minimum length of the active volume was found out. Here we repeat the design criteria and discuss the technical points of the construction of the chamber.

- The system should be able to work at rates as high as 10^{12} photons/mm^2 s.
- It should work in the energy range of 5-20keV.
- It should not attenuate the original photon beam to an unacceptable level: ~5% at higher energies and ~20% at lower energies.
- The precision of intensity measurement should be better than 10^{-4}.
- Largest incident photon beam area: 4X10 mm^2.

3.2. Mechanical Design

The detector is a segmented parallel plate ionization chamber with ultra thin electrodes and windows. Fig.3.2-1 shows the schematic of the detector.

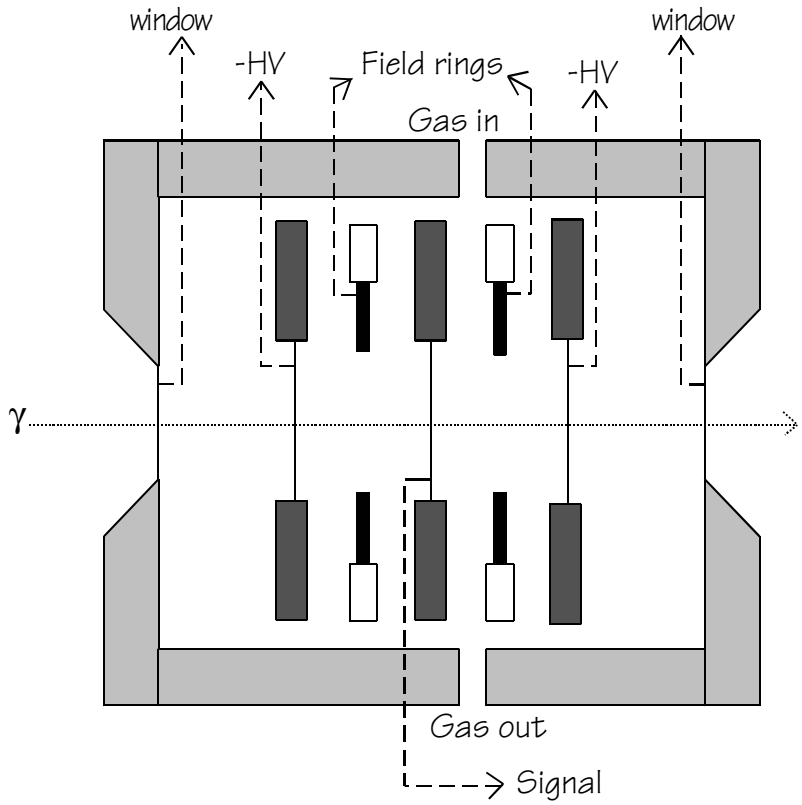

Fig.3.2-1. Schematic of mechanics of beam monitor

The main features of mechanical design of chamber are discussed below.

Ultra thin electrodes and windows

The detector has been so designed that the incident X-ray beam has to pass normally through the electrodes and windows (see fig.3.2-1). As discussed before, a beam monitor should not absorb the incident beam to an appreciable level. To meet this demand, the electrodes and windows of the chamber have been made by ultra thin PET foil (mylar). For all electrodes and windows 6μm thick mylar foil metallized with 0.3μm aluminum has been used. This allows an acceptable proportion of the original low energy beam to pass through without being parasitically absorbed. The disadvantage of using such thin windows is that they can withstand only very small pressure differences and consequently the system can not be operated at high pressure.

The windows are metallized only on inner side to collect charges produced in dead volume of chamber. The electrodes are, however, aluminized on both

sides. A guard ring has been provided on readout electrode to collect leakage current.

The electrical connections of electrodes have been realized through glue and conductive silver paint. The two sides of electrodes were first connected together by thin copper foil which was then glued with the respective electric wire. Conductive silver paint at the joints ensures good electrical connection. Very thin (2mm outer diameter) coaxial cable has been used to carry the ionization current to the PC board.

Fig.3.2-2 shows the percentage absorption of the beam in windows and electrodes. The high absorption at low energies is still under acceptable level. To high energy photons the windows and electrodes are nearly transparent.

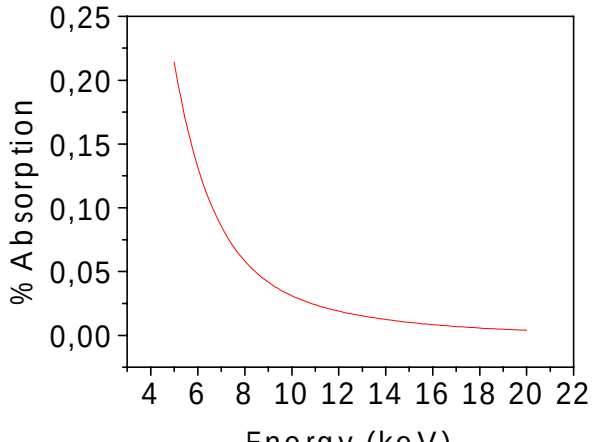

Fig.3.2-2. Percentage absorption of photons in windows and electrodes.

Active and dead regions

The active volume of the detector consists of two cylindrical regions separated by central readout electrode. Each of these regions is 8mm thick and has 7mm radius. The two separate and symmetric active regions bounded by field forming HV electrodes ensure an efficient collection of ions, thus reducing problems caused by space charge. The widths of the dead regions have been kept exactly the same as of the active regions. There are

two advantages of this design. Firstly, since the central readout electrode and the windows are kept at exactly the same potential with respect to the field forming electrodes, therefore no electrostatic force exists between the central electrode and the windows. Secondly, this makes sure that no appreciable mechanical stress is produced on any of the electrodes due to pressure gradients in subsequent regions provided the gas flow is kept uniform throughout the chamber.

Field rings

Two field rings have been provided in active regions to smoothen out the electric field at the edges. These rings are fixed at exactly half way between readout electrode and HV electrode in each region. They are kept at half the potential of field forming electrodes. Field rings have been made by 100μm copper foils. The electrical connections have been made by directly soldering the wires to copper foils.

Vessel

The whole assembly is enclosed in a heavy aluminum vessel having 1cm thick wall. The use of heavy vessel ensures that the system does not vibrate in response to the external sources of mechanical vibration and hence the errors caused by microphony are minimized. Metal screws have been used to support the chamber assembly to one of vessel lids. Gas inlet and outlet have been provided on top of the vessel. The walls of the vessel are 1cm thick and the whole set up has been designed to ensure mechanical stability during operation.

A PC board has been used to provide electrical connections for high voltage and output signal.

3.3. Electronics

High precision measurements with a radiation detector demand low noise and linear electronics. In the following the analog and digital electronics used for the readout of the constructed beam monitor are briefly described.

3.3.1. Analog Electronics

The ionization current generated in the active volume of the detector is proportional to the charge produced which is linearly related to the number of incident photons. Therefore the measured ionization current leads to the determination of intensity of the incident photon beam. In the most simplified case, this ionization current can be directly measured by a precision ampere meter. However, if the current is very low (less than a pA) then it is desirable to first amplify it before recording. A transimpedance amplifier can serve the purpose. Two such devices are shown in figures 3.3.1-1a and b. The output voltage of a conventional transimpedance amplifier (fig.3.3.1-1a) is proportional to the input current, i.e.,

$$V_O = -I_{in} \cdot R_F$$

The feedback resistor R_F determines the transimpedance gain. Very large values of the feedback resistor are needed to get high gain. For example, for an input current of 1nA, a typically used feedback resistance of 100MΩ will produce an output voltage of 0.1V. If the current is of the order of pico amperes then the feedback resistance will have to be increased to a very high value which might be impracticable or very difficult to realize.

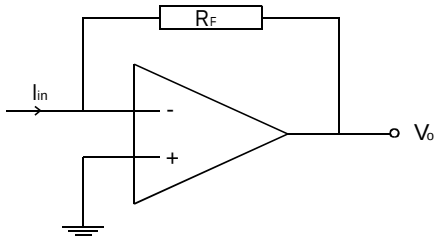

(a)

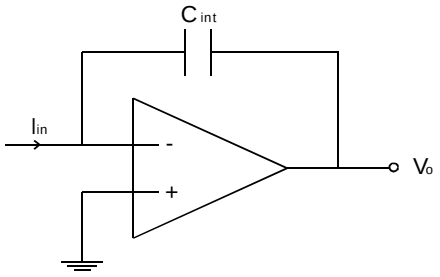

(b)

Fig.3.3.1-1 (a) conventional, and
(b) integrating transimpedance amplifiers.

Fig.3.3.1-1b shows an alternative solution to this design. The output voltage from this *integrating* transimpedance amplifier is given by the transfer function,

$$V_o = -\frac{1}{C_{int}} \cdot \int_0^{\tau} I_{in}(t)dt$$

If the current remains constant during the integration time τ then the output voltage is proportional to the current, i.e.,

$$V_o = -I_{in} \cdot \frac{\tau}{C_{int}}$$

The transimpedance gain in this case is given by the ratio of the integration time to the integration capacitance. A gain equivalent of 1GΩ can be achieved easily with an integration time of 100mS and an integration capacitance of 100pF. This will give an output of 1 volt for an input current of 1nA while a 1pA current in this case will give an easily measurable output of 1mV.

The second advantage of such devices is that the height of the output voltage can be varied according to the specific requirement by varying the integration time or the integration capacitance. The integration time can be controlled by the external switching unit in switched integrators while the integration capacitance can be changed in the PC board for the integrator. This provides more flexibility in the system.

The third advantage is the lower overall noise of such devices as compared to the conventional transimpedance amplifiers. The use of integration capacitor instead of feedback resistor lowers the leakage current and eliminates the thermal noise of the resistor.

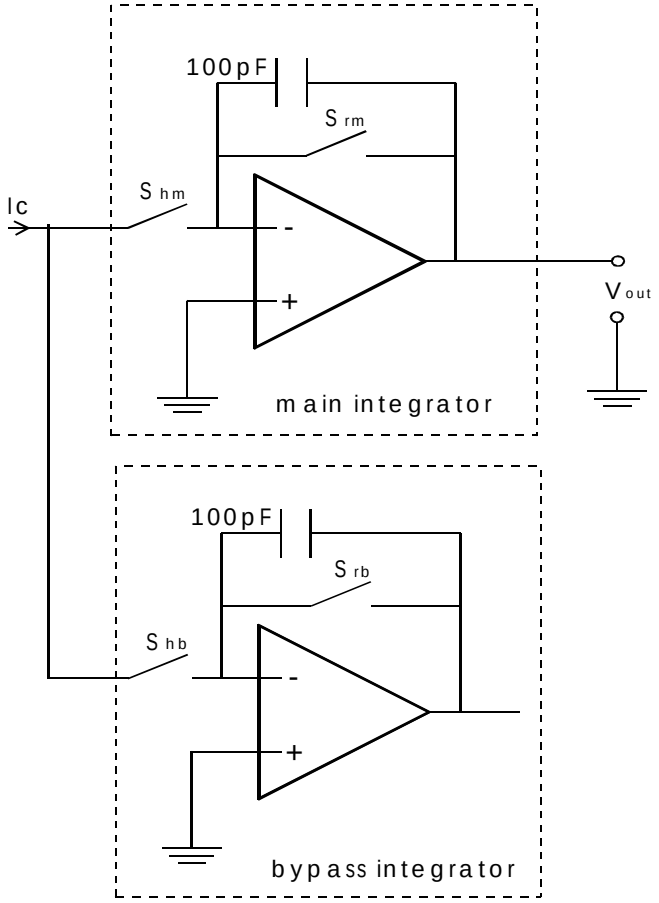

Fig.3.3.1-2. Sketch of integration setup of beam monitor.

In the constructed beam monitor, the output current is integrated on a commercially available precision transimpedance integrating amplifier

IVC102 of BURR BROWN. The sketch of the integration setup is shown in fig.3.3.1-2.

IVC102 is a switched integrator which facilitate the variation of integration time with the help of hold and reset switches (S_h and S_r respectively). However the hold switch is internally clamped with diodes which can withstand a maximum of 200mV before being forward biased. Therefore during the reset time when hold switch is open and the charge accumulates on the capacitance of detector and connecting cables, the resulting voltage drop should not exceed 200mV, otherwise the integrator will start unexpectedly integrating again and there will be some degree of uncertainty in the integration time and hence the measured intensity. To overcome this difficulty, another integrator has been used in parallel with the main integrator. The second one (termed as bypass integrator in fig.3.3.1-2) has been used to bypass the charge collected during reset period of the main integrator. In this way, no charge is ever accumulated on the capacitance of detector and the connecting cables. Fig.3.3.1-3 shows the timing diagram to drive both the integrators.

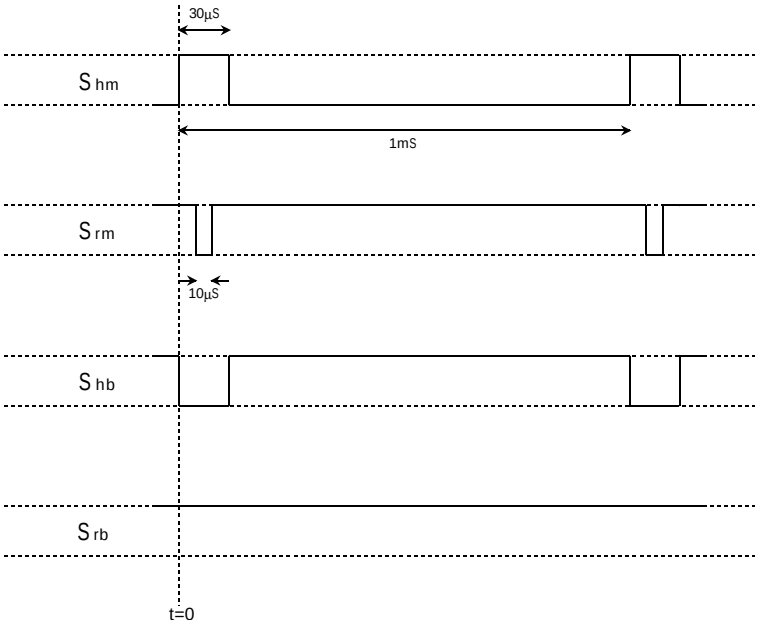

Fig.3.3.1-3. Timing diagram of current integration.

As shown in fig.3.3.1-3, the timing sequence of the hold switch of the bypass integrator is exactly opposite to that of the main integrator. The reset switch of the bypass integrator is kept always closed so that the current is instantly grounded. The information during this time is therefore lost and the recording is not in the real sense dynamic. But this loss of information does not affect the measurement while the system can be accordingly calibrated. In case of relative intensity measurements, the constant width of timing pulse ensures that the information lost during the resetting time of the main integrator does not influence the precision of the measured intensity.

The integrator can be used to integrate both positive or negative currents, i.e., either positive ions or electrons can be collected by the central readout electrode of the chamber. Fig.3.3.1-4 shows the output of integrator for a constant current input.

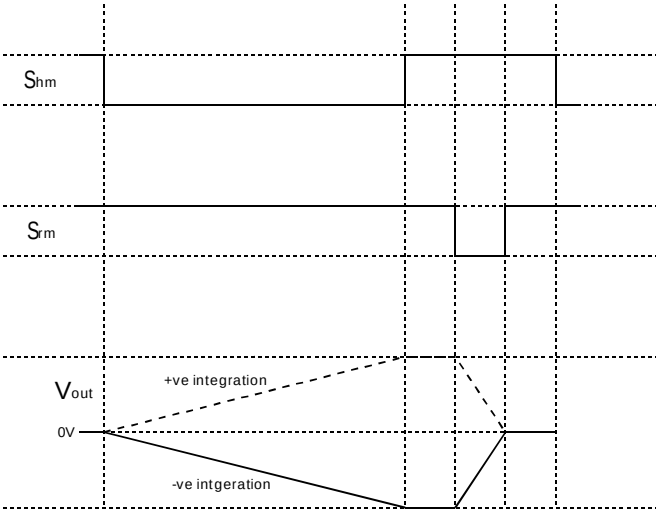

Fig.3.3.1-4. Integration of positive and negative currents

3.3.1.1. Precision Limits of Current Measurements

Different sources of noise contribute to the overall noise of the integrator. The most appreciable among those are the input offset voltage, input bias current and switch charge injection. In the following we briefly discuss each of these

sources of error and methods adapted to reduce their effect on measurements.

Input Offset Voltage

There are two types of input offset voltages, detector offset voltage and Op Amp offset voltage. The detector offset voltage is the voltage induced due to accumulation of charge on the capacitance of detector and connecting cables during the integration time (switch S_{hm} open). As discussed above, no error in measurement is caused if this voltage does not increase above 200mV. Since we have used a bypass integrator which does not allow any charge accumulation during this time therefore detector input offset voltage is zero. The integrator's Op Amp offset voltage is intrinsic to the integrator's design and is always there. Its effect can, however, be decreased by two-point measurement scheme described later in this chapter.

Input Bias Current

The integrator used has a very small input bias current. But to achieve this, the printed circuit layout must be carefully designed such that no surface or volume leakage currents flow into the input of the integrator. The input bias current of the integrator depends exponentially on temperature. At 25 ^{0}C it is approximately 100fA which is small compared with the typical ionization current of the order of a nA. If this value remains constant then it induces no error in the relative measurement. But there are always some fluctuations around this mean value caused by the thermal fluctuations. The exact amount of temperature fluctuations depend on the operating conditions but are not expected to be very large because in that case the large changes in density of the gas will make the system too unstable to be properly used (see section on Stability). If we suppose 5% change in the input bias current due to temperature fluctuations from one measurement to the next, then at 25 ^{0}C

the relative error in the ionization current of 1nA will be $5X10^{-6}$ which is of course very small and can be ignored.

Switch Charge Injection

The switch charge injection is the most significant source of error. It depends primarily on the source capacitance. The capacitance of the beam monitor and connecting cables is approximately 10pF. At this value the voltage difference caused by charge injection through hold switch is 12mV and through reset switch is 4mV. These values are not insignificantly small as compared to the typical voltage signal of 1 to 3 volts and therefore must be somehow reduced. The two-point difference measurement method has been used with the beam monitor to reduce the effect of switch charge injection. This method has been described below.

3.3.1.2. Data Readout Sequence

The effect of different sources of noise on the integrator output is shown in fig.3.3.1.2-1. The transfer function offset voltage is the voltage measured during the hold period at P2. Since the opening and closing charge injections of hold switch are very nearly equal and opposite (the ramp due to input bias current is exaggerated) therefore the transfer function offset voltage is dominated by the charge injection of reset switch opening and Op Amp offset voltage. If the data is read at points P1 and P2 then the difference P2-P1 reduces offset due to Op Amp offset voltage and reset switch charge injection. As already discussed, the ramp due to input bias current (exaggerated in fig.3.3.1.2-1) is very small and contributes to the overall noise and error of the system.

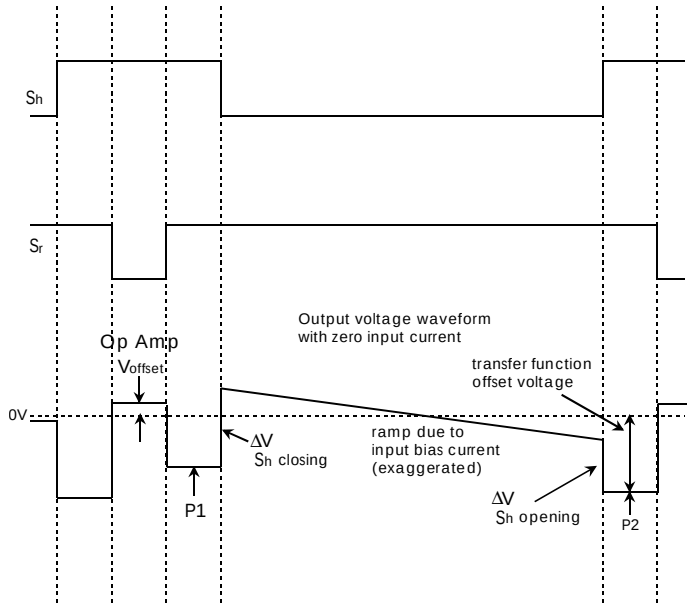

Fig.3.3.1.2-1. Effect of different error sources on output waveform at zero input current.

3.3.1.3. Noise of Analog Electronics

The total noise of the integrator is given in data table as a function of source capacitance and integration capacitance. For the beam monitor with roughly 10pF capacitance, the output noise equivalent voltage is approximately 8μV with integration capacitance of 100pF. This corresponds to an equivalent ionization current of 0.8pA for 1mS integration time. In a chamber filled with argon at normal pressure, this is equivalent to roughly 13 absorbed photons of 10keV.

3.3.1.4. Linearity of Analog Electronics

It is obvious that for high precision measurements the electronics should behave linearly with respect to incident photon intensity. The linearity of analog electronics was checked using the set up shown in fig.3.3.1.4-1.

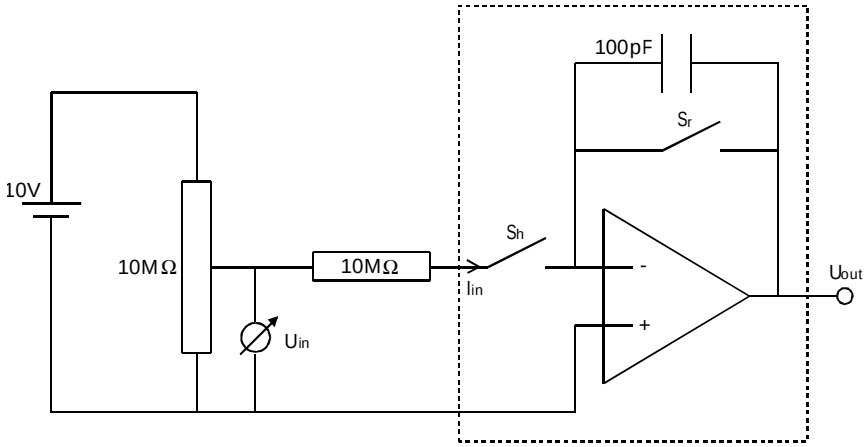

Fig.3.3.1.4-1. Setup for linearity check of analog electronics.

The current flowing into the integrator could be varied by the variable resistance. The voltage at the input stage U_{in} was measured by a digital voltmeter. The output voltage was measured by an oscilloscope.

The only source of noise at the input stage is the thermal noise of the resistors, given by,

$$\sigma_{I_{th}} = \sqrt{\frac{4 \cdot k \cdot T}{R} \cdot \Delta f}$$

Where k is the Boltzman's constant, T is the temperature in Kelvin, R is the resistance in Ohms and Δf is the frequency bandwidth. For the frequency bandwidth of 1kHz and at normal temperature of 25 ^{0}C, the thermal noise current of the 10MΩ resistance is 1.28pA. This is negligible as compared to the expected minimum current of the order of a nano ampere caused by synchrotron radiation. The input current can be converted into equivalent number of absorbed photons by the following relation,

$$N_{eqv} = \frac{I_{in} \cdot \tau}{\frac{E_\gamma}{W} \cdot e}$$

Where τ is the integration time, W is the energy needed to produce an electron ion pair by photons of energy E_γ; I_{in}(=U_{in}/R) is the input current in amperes, and e is the electronic charge in coulombs. Fig.3.3.1.4-2 shows the

result of the linearity test. The analog electronics did not show any deviation from linearity in the range of achievable current.

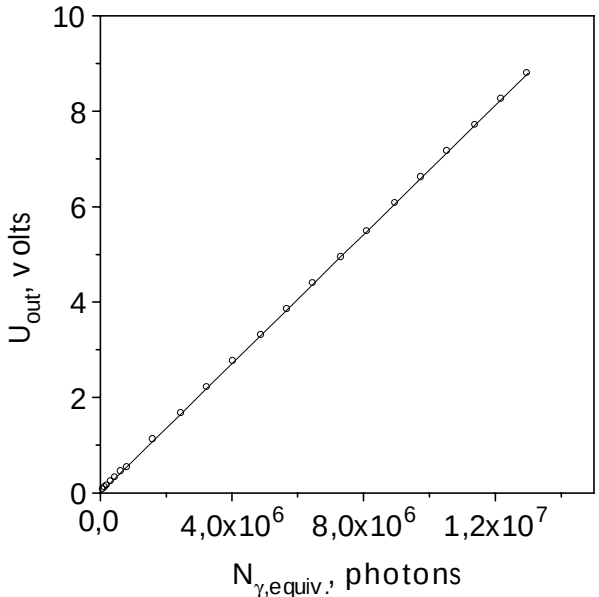

Fig.3.3.1.4-2. Linearity of analog electronics.

3.3.2. Digital Electronics

The digital electronics plays an equally important role in data acquisition. In the following sections a brief description of digital electronics set up of beam monitor is given.

3.3.2.1. Analog to Digital Converter

The output voltage can be measured by any suitable instrument such as an oscilloscope. It is, however, desirable to first convert this analog voltage into digital word which could be read and recorded by a computer for further processing. In present work, a commercially available 16 bit analog to digital converter ADS7805 has been used. The block diagram of the integrator card is shown in fig.3.3.2.1-1. A transimpedance amplifier provided at the input stage of ADC card serves the purpose of amplifying the output voltage of the

integrator to exploit the full dynamic range of the ADC. A 1k buffer has been provided at the output of ADC to facilitate digital data readout.

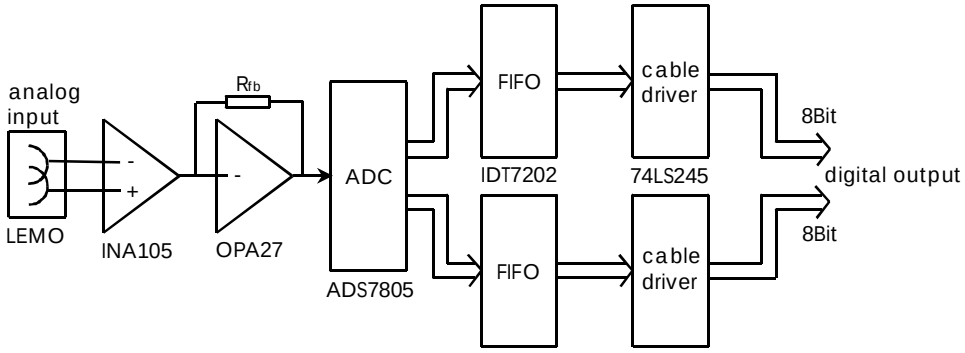

Fig.3.3.2.1-1. Simplified block diagram of ADC card.

The noise of the ADC for a single measurement is calculated as follows,

$$\sigma_{dig} = \frac{1LSB}{A \cdot \sqrt{12}}$$

Where the least significant bit is denoted by LSB, A is the amplification factor at the input stage of ADC card and the numerical factor in denominator is the usual error factor for block function.

For the ADC card described above, this turns out to be 26.4μV.

3.3.2.2. Digital Control Signals

A number of digital control signals are needed to drive the integrator and ADC. A programmable NIM controller has been used for this purpose. The controller works with a 1MHz crystal oscillator and can be programmed according to the need by 1k EPROMS.

The complete block diagram of the electronics chain of the beam monitor is shown in fig.3.3.2.2-1.

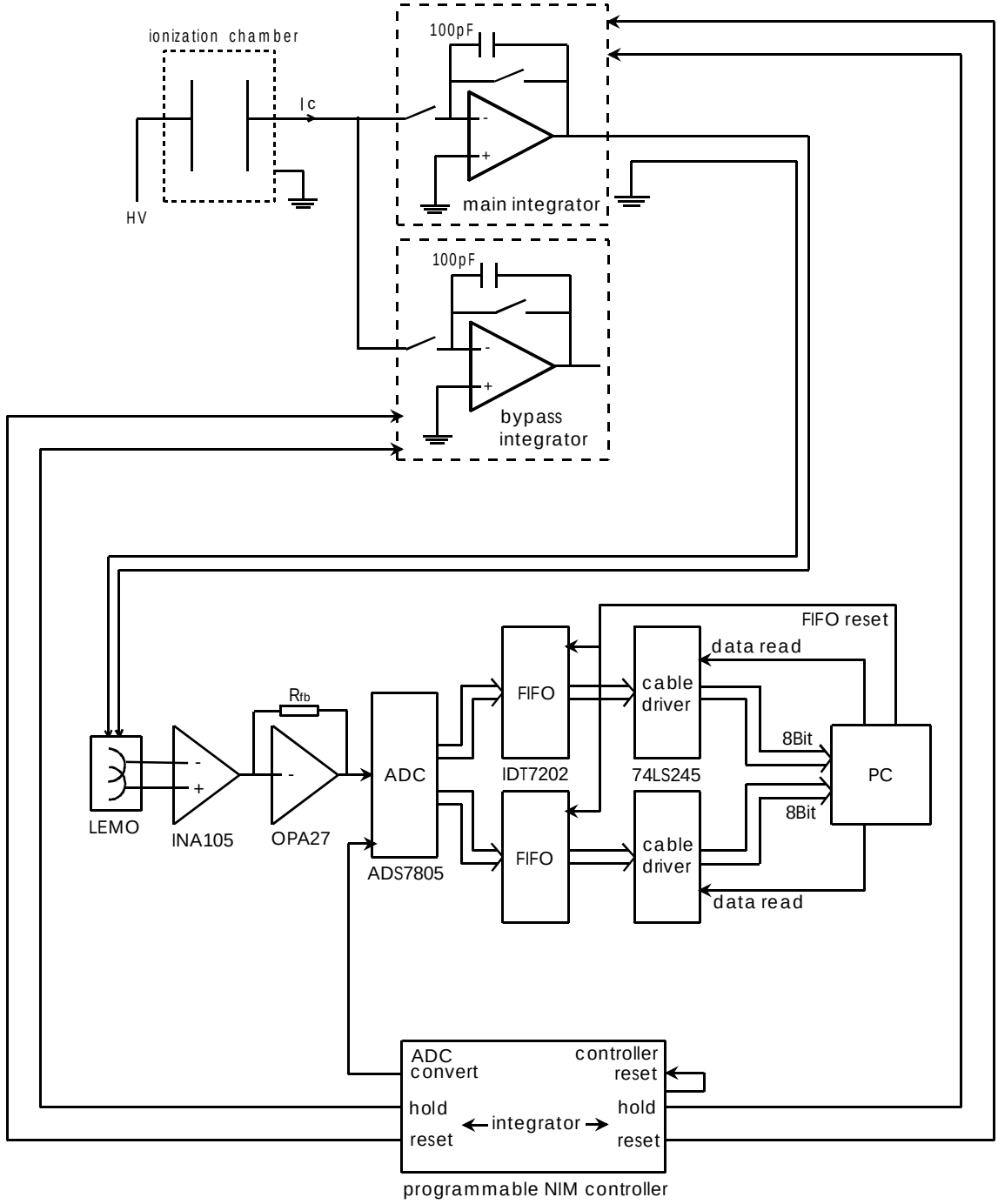

Fig.3.3.2.2-1. Block diagram of the complete electronics chain.

3.3.3. Overall Electronics Noise

The overall electronics noise is the quadratic sum of the fluctuations due to analog and digital electronics, i.e.,

$$\sigma_{elec}^2 = \sigma_{anal}^2 + \sigma_{dig}^2 + \sigma_{switch}^2$$

Here the last term on RHS represents the switching noise. If we assume that the two point measurement scheme (described in section 3.3.1.2) reduces the effect of switching noise to insignificant level then the overall noise is the quadratic sum of integrator noise and ADC noise. In this case we get,

$$\begin{aligned}\sigma_{elec}^2 &= (8)^2 + (26.4)^2 \\ &= (27.6)^2 \qquad (\mu V)^2\end{aligned}$$

4. Efficiency of the System

There are different standard criteria for judging the performance of a detection system. Their utility in judging the performance depends on the particular design criteria of the system and its usage. Here we will discuss two of these criteria, namely, quantum efficiency and detective quantum efficiency.

4.1. Detective Quantum Efficiency and Quantum Efficiency

The detective quantum efficiency is a parameter which can be used to determine the efficiency of the system with respect to the noise at input and output stages. Mathematically it is defined as the square of the ratio of signal to noise ratio at the output to signal to noise ratio at the input of the system, i.e.,

$$DQE = \left(\frac{SNR_{out}}{SNR_{in}} \right)^2 \qquad (4.1\text{-}1)$$

Since the incident photons follow Poisson statistics, therefore at the input stage the signal to noise ratio can be calculated as,

$$SNR_{in} = \frac{N_{in}}{\sigma_{poi}} = \frac{N_{in}}{\sqrt{N_{in}}} = \sqrt{N_{in}}$$

The measured signal depends linearly on the number of photons absorbed in the detector. This can be determined by multiplying the quantum efficiency of the detector with the incident number of photons,

$$N_{out} = QE \cdot N_{in}$$

Quantum efficiency (QE) is a parameter which determines the fraction of photons absorbed in the active volume of chamber to the total number of

incident photons. It depends on the mechanics of the chamber and the filling gas used. For the constructed beam monitor this was found to be,

$$QE = \exp(-\mu_g \cdot \rho_g \cdot x_{gd}) \cdot \exp(-3\mu_{Al} \cdot \rho_{Al} \cdot x_{Al}) \cdot \exp(-2\mu_{my} \cdot \rho_{my} \cdot x_{my}) \cdot \left(1 - \exp(-\mu_g \cdot \rho_g \cdot x_g)\right) \cdot \left(1 + \exp(-2\mu_{Al} \cdot \rho_{Al} \cdot x_{Al}) \cdot \exp(-\mu_{my} \cdot \rho_{my} \cdot x_{my}) \cdot \exp(-\mu_g \cdot \rho_g \cdot x_g)\right) \quad (4.1\text{-}2)$$

Here μ is the mass absorption coefficient, ρ is the mass density and x is the thickness of the respective materials characterized by subscripts. Filling gas is represented by g, Aluminum by Al, Mylar by my, and gap of dead region by gd. Since the mass absorption coefficient is energy dependent therefore the quantum efficiency depends on energy of incident photons.

The fluctuations in the output signal of the detector is given by,

$$\sigma_{out} = \left(\sigma_{poi}^2 + \sigma_{add}^2\right)^{1/2}$$

$$= \left(QE \cdot N_{in} + \sigma_{add}^2\right)^{1/2}$$

Here σ_{add} is the additional noise of the system, e.g., electronics noise, digitization error etc.

The signal to noise ratio at the output is then given by,

$$SNR_{out} = \frac{N_{out}}{\sigma_{out}} = \frac{QE \cdot N_{in}}{\left(QE \cdot N_{in} + \sigma_{add}^2\right)^{1/2}}$$

The square of the ratio of signal to noise ratio at output to signal to noise ratio at input gives the required detective quantum efficiency of the detector,

$$DQE = \frac{QE}{1 + \frac{\sigma_{add}^2}{QE \cdot N_{in}}} \quad (4.1\text{-}3)$$

Hence DQE is a monotonically increasing function of incident number of photons and reaches it's limiting value of quantum efficiency (see fig.4.1-3).

The QE of the constructed beam monitor for the energy range of interest is shown in fig.4.1-1. The filling gas is 90%Ar +10%CH_4.

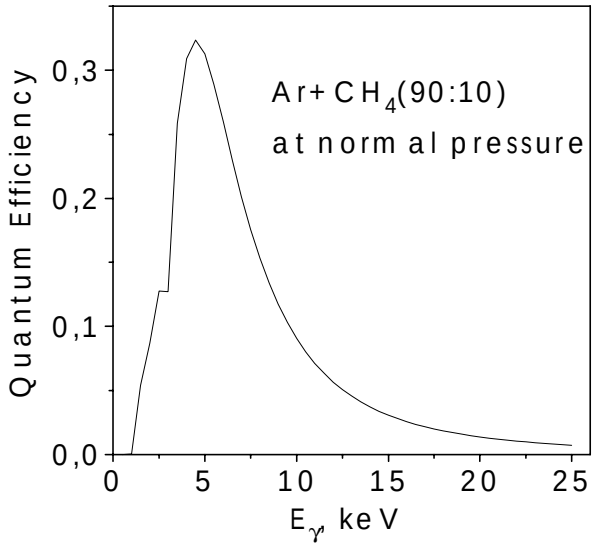

Fig.4.1-1. Quantum efficiency of the detector as a function of incident photon energy.

At energies lower that 5keV the higher parasitic absorption in the windows and gas in the first end gap of the detector decreases the quantum efficiency rapidly. The maximum efficiency for the gas used is 31% at 5keV. At 20keV the efficiency is roughly 1.37%. To see whether this low efficiency is a bottleneck in precision measurement at typical photon rates on a synchrotron facility, the approximate output signal for this case has been calculated when 10^{10} photons/S arrive at the entrance window of the detector.

The number of photons being absorbed per second is 1.37 X 10^8. This is equivalent to 1.05 X 10^{11} electron-ion pairs being generated per second. This gives an ionization current of 16.9nA and an output voltage of 169mV for 1mS integration time and 100pF integration capacitance. The corresponding Poisson fluctuation is equivalent to 14.4μV and the total electronics noise and

digitization error is 27.6μV, giving a total fluctuation of 31.1μV. And hence the precision of single measurement in this case is 1.8 X 10^{-4}. This shows that at high rates of incident photons, the low quantum efficiency of the system does not pose a problem for precision of measurement provided the contamination in the system is kept negligible.

Fig.4.1-2 shows the computed quantum efficiency for different gas mixtures of argon and methane as a function of energy of incident photons. At lower energies (around 5keV), even only methane can be used. It has the advantage of absorbing small number of photons, thus leaving larger unattenuated portion of the x-ray beam for further experimentation. At higher energies 100% methane in unsuitable because of extremely small quantum efficiency and therefore a mixture of argon and methane can be used.

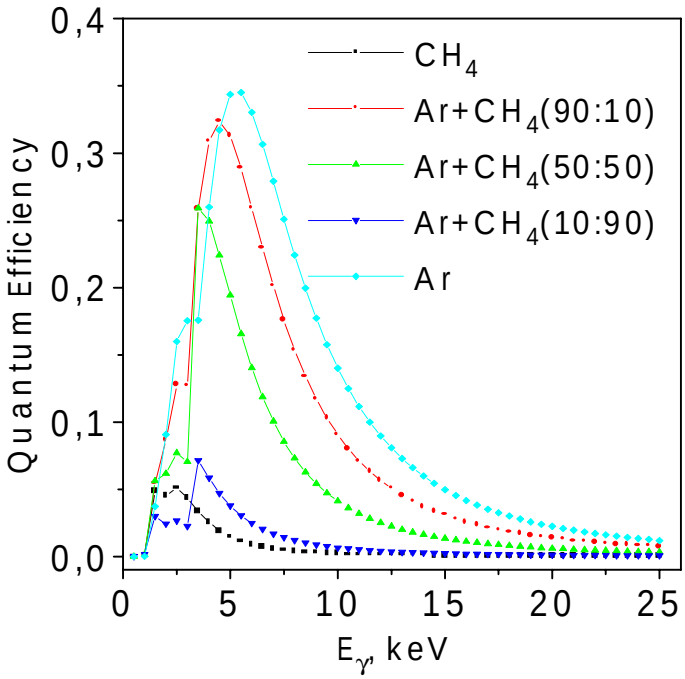

Fig.4.1-2. Quantum efficiency of the beam monitor for different gas mixtures.

The detective quantum efficiency of the beam monitor as a function of incident photons for different photon energies is shown in fig.4.1-3.

It can be seen that the beam monitor is not suitable for incident photons rates of less than 10^5 per second. This can also be intuitively understood while the ionization chamber built here absorbs a small number of photons from the original beam of x-rays. For an incident flux of less than10^5 per second, the number of absorbed photons is so low that an appreciable signal will not be produced and consequently the measurements will not be very precise.

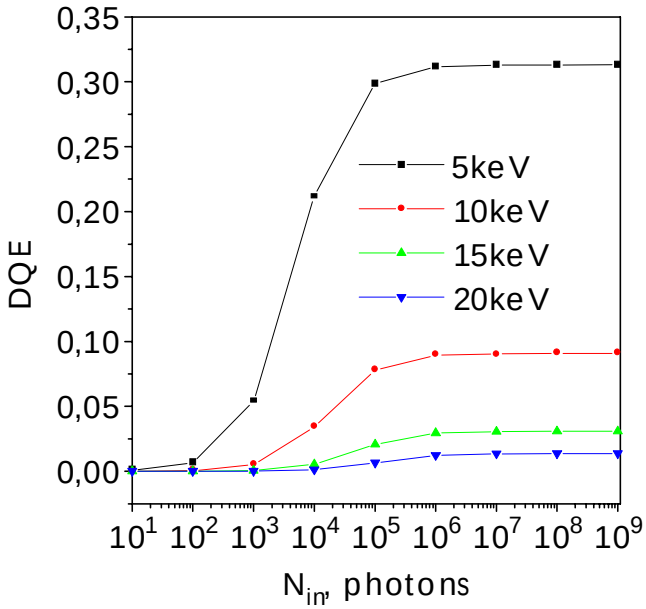

Fig.4.1-3. Detective quantum efficiency of beam monitor at different incident photon energies.

5. Measurements and Data Analysis

The aim of this work was to study the quantum fluctuations in the segmented ionization chamber to be used as a beam intensity monitor for synchrotron radiation experiments. It is, however, necessary first to check closely the linearity of the system and measure the ionization chamber plateaus at respective x-ray intensities before studies related to quantum fluctuations can be performed. In the following a brief description of the necessary test measurements performed with the constructed chamber is presented.

5.1. Experimental Arrangement

The experimental setup is shown in fig.5.1-1. A 2kW crystallographic x-ray tube with molybdenum anode, with a characteristic energy of 17.44keV, was used for test measurements. The beam was collimated with a very narrow collimator which was made by drilling a 0.8mm diameter hole in 10mm thick lead and 5mm thick aluminum sheets. The intensity of x-rays could be controlled by tube current because from previous experience it was known that, for the particular tube used, the intensity is directly proportional to the tube current. For all measurements the HV on tube was kept at 25kV to keep the contribution of Bremsstrahlung small.

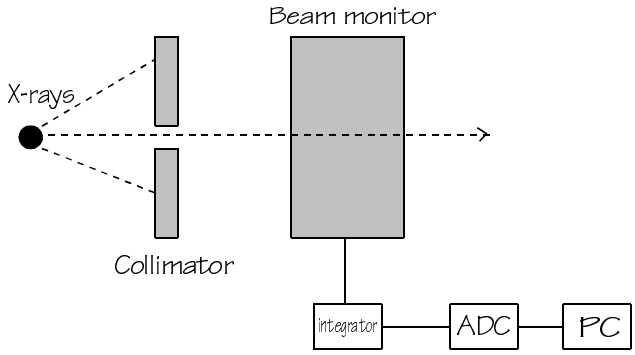

Fig.5.1-1. Experimental setup

5.2. Choice of Gas

The filling gas in the chamber should be capable of generating a sufficiently large number of electron-ion pairs in order to ensure good signal to noise ratio. At the same time the beam should not be attenuated to an undesirable level. In general an absorption of 5-20% of original beam is considered acceptable. For a particular experiment, the choice of gas depends on the required resolution and acceptable attenuation of beam. During this work the chamber was tested with gas mixtures of 95%Ar+5%CO_2 and 90%Ar+10%CH_4. Since the pressure in the chamber could not be raised due to very thin windows, therefore use of a conversion gas having very small attenuation coefficients (e.g. Helium) was not possible as it would have produced a very small number of electron ion pairs. On the other hand, use of a heavier gas, for example xenon, would attenuate the beam to unacceptable levels (above 20%). The attenuation coefficients of argon are neither very small nor very large and therefore it was chosen for the experimentation with the beam monitor. Another plus point with argon is its low cost and consequently easy availability. The use of another gas with argon serves to "dilute" the argon and hence the attenuation can be controlled by varying the concentration of this plus gas (see section on quantum efficiency for details).

The parasitic electron capture by admixtures and contaminants leads to the deterioration of the signal and must be minimized. The electron capture probability in CO_2 is higher as compared to CH_4 (see Appendix-D). In fact the mean electron capture time in carbon dioxide is a fraction of a millisecond (under normal conditions for thermal electrons) and therefore if there is an appreciable percentage of this gas in the chamber, it will lead to an appreciable loss of electrons and consequently the ionization current will decrease. To check this, the beam monitor was tested with a mixture of 90% argon and 10% carbon dioxide (see section 4.3.1). For all the other tests a gas mixture of 90% argon and 10% methane was used while it was known that

methane shows the lowest electron capture probability [Sitar B. et al., 1993] as compared to other standard admixtures.

The purity of the filling gas is also very important because even small amounts of oxygen or water lead to deterioration of signal. Physically this can be understood by the fact that the mean electron capture time in these gases is some hundreds of nanoseconds [Sauli 1977]. The filling gas is also contaminated by diffusion through the thin mylar windows and degassing of inner parts of the chamber. The slow degassing of the inner parts of the chamber (mainly due to gases trapped in the holes) can be lowered if the chamber is flushed with the filling gas for some days before being used in experiments.

5.3. Basic Tests of Ionization Chamber

The most basic condition for a detector to work in ionization chamber region is that it should collect all the charges produced in the active volume and there should be no (or negligible) losses. This means that the measured ionization current should be independent of the voltage applied to the detector. The second condition is that the behavior of the system should be linear with respect to intensity of incident photons. In the following, the tests to check these two necessary conditions have been briefly described.

5.3.1. Ionization Chamber Plateau

Fig.5.3.1-1 shows the ionization chamber plateaus for different x-ray intensities. Careful designing, positioning and mounting of electrodes of chamber is necessary to ensure parallel electric field lines in the conversion regions and to enable a proper gas flow. It is necessary that the electric field lines are kept parallel in the outer cylindrical region of the active part of the chamber in

order to effectively collect the charges produced there (for example by photon beams of large area or by improperly collimated photon beam). In order to ascertain parallel field lines in the active volume, two field rings have been provided in each active region. Furthermore, care was taken to place all the electrodes parallel to each other. The gas flow in the chamber should not produce any pressure gradient in any region because this will change the active length and hence the number of charge pairs being produced will fluctuate. To circumvent this, the lengths of all the four regions have been kept equal to each other and a number of holes have been provided symmetrically to facilitate the proper gas flow. Another factor which plays an important role is the choice of filling gas. The electronegative impurities in the gas tend to capture the electrons causing loss of information. Therefore it is necessary that the system is kept free of such electronegative impurities. For the measurements presented here the chamber was operated with two different gas mixtures. A mixture of 90%Ar+10%CH_4 resulted in plateau slopes of less than 2% per 1000 volts while a mixture of 95%Ar+5%CO_2 produced slopes of roughly 3% per 1000 volts. The larger positive slope in the later case was mainly due to the high electron capture probability of carbon dioxide (see Appendix-C). This effect is followed by the following two reactions,

$$e^- + YZ \rightarrow (YZ)^{-*} \quad , \quad (YZ)^{-*} + X \rightarrow (YZ)^- + X + energy$$

$$e^- + Z + X \rightarrow Z^- + X + energy$$

In the first process, Z can be some electronegative impurity such as oxygen and X represents carbon dioxide or some other molecule which is capable of taking all the excess energy. When the applied electric field is small, the electron capture by carbon dioxide is large and consequently the loss of ionization current is also large (this happens since the recombination probability for negative ion is larger than that of electron). This loss decreases as the voltage applied to the chamber is increased and hence the ionization current increases. Thus, such a gas is not suitable for use as admixture in the beam monitor where high precision is required. Therefore in all the experiments performed later a mixture of argon and methane was used.

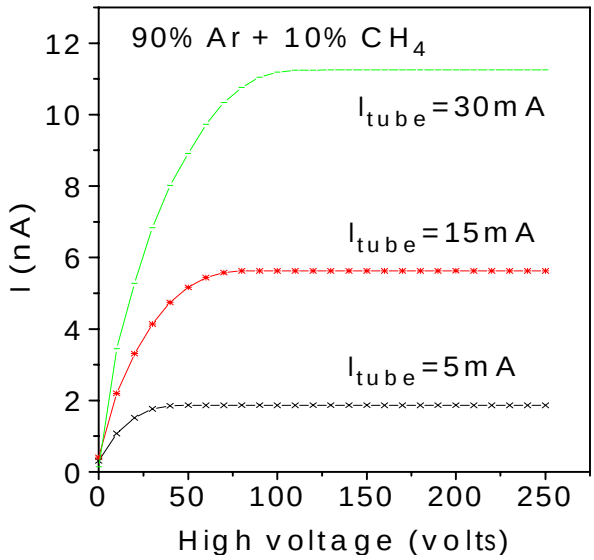

Fig.5.3.1-1. Ionization chamber plateaus at different x-ray tube currents.

5.3.2. Linearity

For proper performance of the monitor it is necessary that it behaves linearly with respect to incident photon flux. From previous experience it was known that the photon flux from the x-ray tube being used depends linearly on the tube current. To check the linearity of the chamber, measurements were done with respect to x-ray tube current. A series of 1024 readings were taken at each step of x-ray tube current and their average was converted into ionization current by the conversion factors of ADC and integrator,

$$< I_{ion} >= \frac{(10.17 \times 10^{-5}) \cdot < N_c > \cdot \tau}{C}$$

Where N_c represents the average ADC counts, $\tau=10^{-3}$ second is the integration time and $C=100X10^{-12}$ Farads is the integration capacitance. The conversion factor of $10.17X10^{-5}$ converts the ADC counts to volts.

For all measurements the chamber was biased at 200 V using a stable high voltage supply. Fig.5.3.2-1 shows the result of these measurements. No deviation from linearity was found up to the achievable intensity of X- rays.

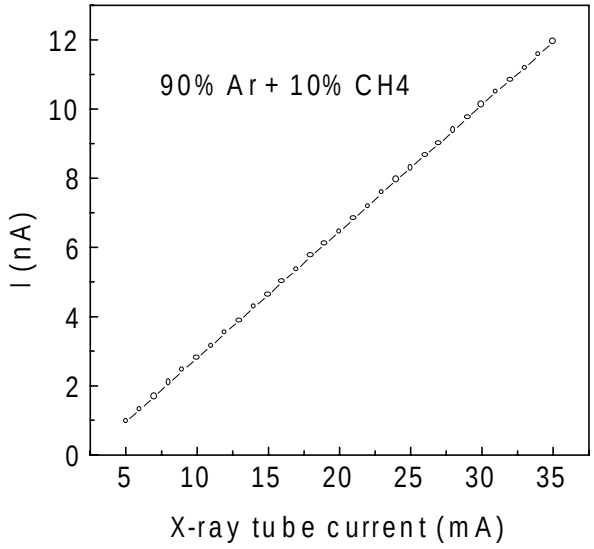

Fig.5.3.2-1. Linearity of chamber signal

This shows that the system as a whole behaves linearly with respect to incident photon intensity. Since the linearity of the analog electronics has already been established (see fig 3.3.1.4-2), therefore from the above result it can be concluded that the performance deteriorating effects, such as, space charge effect (see Appendix-A), contamination in the detector (see Appendix-C) and recombination losses (see Appendix-D) do not significantly contribute to destroy the linearity of the system.

5.4. Quantum Fluctuations

The fluctuations in number of photons absorbed in the active volume of the chamber lead to the fluctuations of the measured ionization current. The Poisson nature of high intensity x-ray beams make it easy to theoretically compute these fluctuations. However experimentally it is not directly possible to measure the quantum fluctuations from the data obtained from an ionization chamber. The reason lies in the fact that in ionization chambers

operating in integration mode, what is measured is the mean deposited energy during the integration time. The fluctuation of this mean deposited energy is, however, a measure of the total fluctuations due to all sources (Poisson, electronics, contamination in the filling gas). The Poisson fluctuations are imbedded in the fluctuations caused by readout electronics and other sources. If the noise due to electronics and other sources is independent of the incident photon intensity, then the variance of the measured data should behave linearly with respect to the respective mean (see section 5.4.3). This gives a method to determine whether the system works at the limit of quantum noise or not. In the following we look briefly at the steps taken to explore this possibility.

5.4.1. Data Filtration

The quantum fluctuations in the data can not be properly studied if the data contains strong fluctuations due to other sources. Therefore, if there are other noise sources, e.g., the x-ray setup itself, then the data must first be filtered before analysis could be properly performed. The x-ray source used in these experiments is known to have fluctuations at nX100 Hz (n=1,2,...) embedded in some unknown but small ripples. Fig.5.4.1-1a and b show a sampled data sequence and its corresponding Fourier transform respectively.

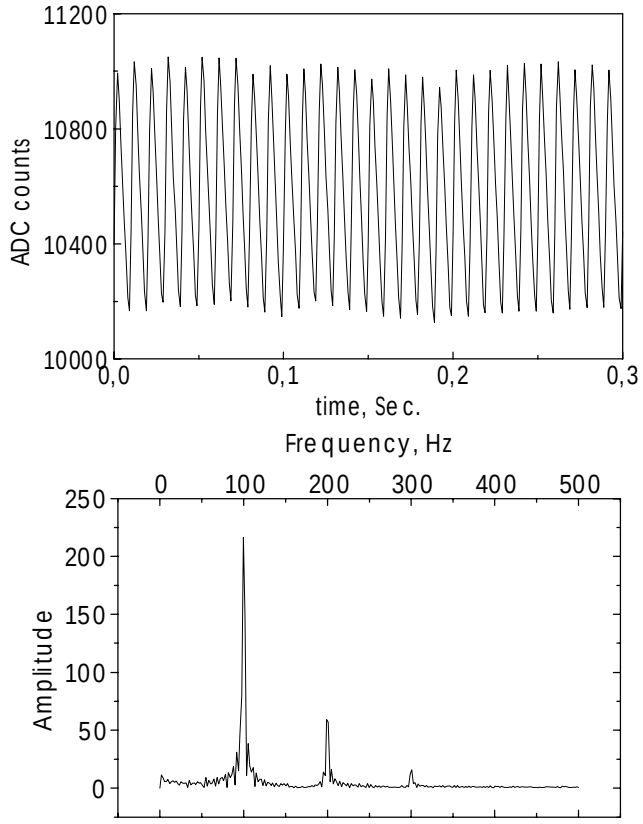

Fig.5.4.1-1. (a)above, sampled data sequence and (b) its Fourier transform.

The nX100 Hz fluctuations seen in the Fourier transform of the sampled data (Fig.5.4.1-1b) probably come from a rectifying circuit in the electronics of the x-ray tube and hence can not be directly suppressed. The amplitude of these fluctuations was found to depend non-linearly on the x-ray tube current (see fig.5.4.1-2).

This strong non-linearity makes it almost impossible to study the underlying small Poisson fluctuations. Therefore the data had to be filtered before being analyzed for quantum fluctuations.

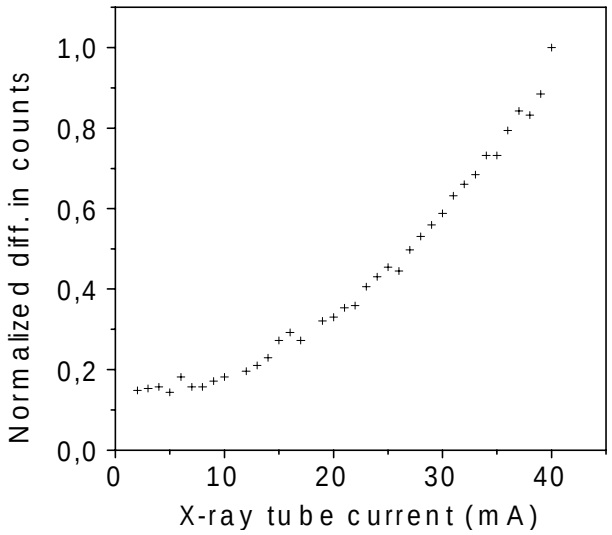

Fig.5.4.1-2. Nonlinear behavior of the difference of maximum and minimum signal with respect to the x-ray tube current.

The filtration was performed off line. The Fourier transform was first taken and the widths of fluctuations at nX100 Hz were identified. The complex variables of the Fourier transform were then filtered using the following band stop filter,

$$g(\nu)=\begin{cases}1 & 0\le\nu\le\nu_1\\ 0 & \nu_1\le\nu\le\nu_2\\ 1 & \nu_2\le\nu\le\nu_{nyq}\end{cases}\quad \text{for all nX100 Hz, n=1,2,...} \qquad (5.4.1\text{-}1)$$

Here ν_{nyq} is the Nyquist frequency and is equal to 500Hz for 1mS data sampling time. The widths 0-ν_1, ν_1-ν_2 and ν_2-ν_{nyq} were chosen by inspecting the Fourier transforms of the measured data.

The resulting data was then inverse Fourier transformed to get the filtered time series data. Fig.5.4.1-3 a and b show a sampled time series data before and after filtration respectively.

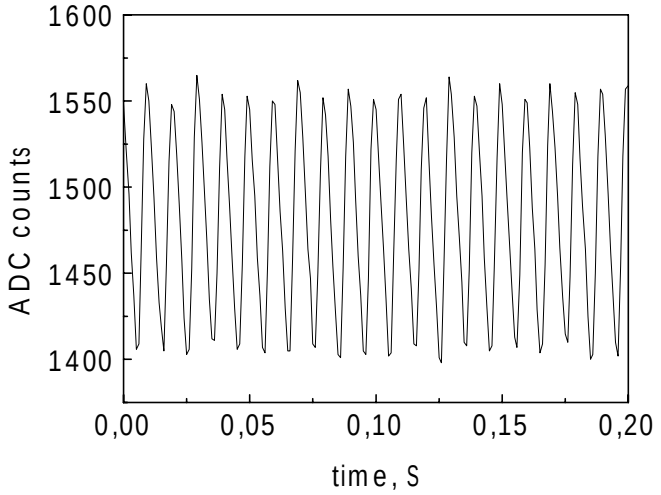

(a)

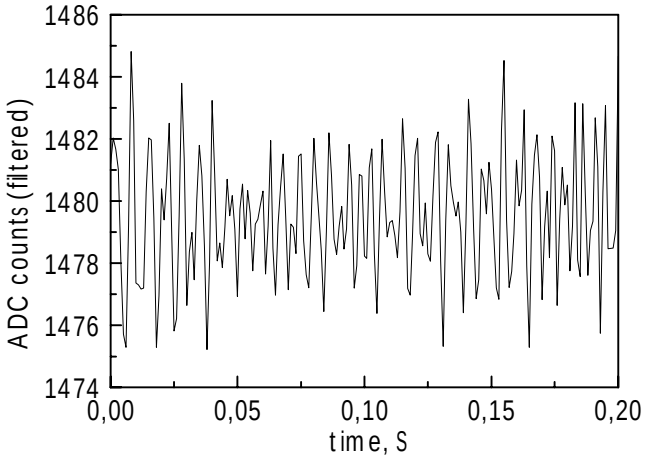

(b)

Fig.5.4.1-3. Time series data (a) before and (b) after filtering.

The small temporal ripples in the photon flux of the x-ray tube used were not touched during the filtration process. Firstly because they were inseparably imbedded in the natural fluctuations and secondly from past experience it was know that their amplitude is not significantly large.

As explained in chapter-6, the gas flow during these experiments was realized through a long gas tube (~10m) at the outlet of the beam monitor. A bubbler was not used because it exerts a back pressure on the gas inside the chamber thus fluctuating the active length of the chamber by a frequency which depends on the flow rate of the gas. This fluctuates the measured

ionization current by the same frequency because the number of gas molecules available for the generation of electron ion pairs fluctuates. When bubbler was used, the Fourier transform of the data showed a frequency of 1-5Hz which disappeared as the bubbler was replaced by the long gas tube.

5.4.2. Spectrum of Incident and Absorbed Photons

In order to find the effective energy of absorbed photons and noise of the system from the measurements, it is necessary to know the spread in the spectrum of absorbed photons. However the spectrum of absorbed photons can only be computed if one knows the spectrum of incident photons. The spectrum of the x-ray tube used in the experiments with beam monitor has been measured by an argon filled proportional counter. The experimental set up is shown in fig. 5.4.2-1.

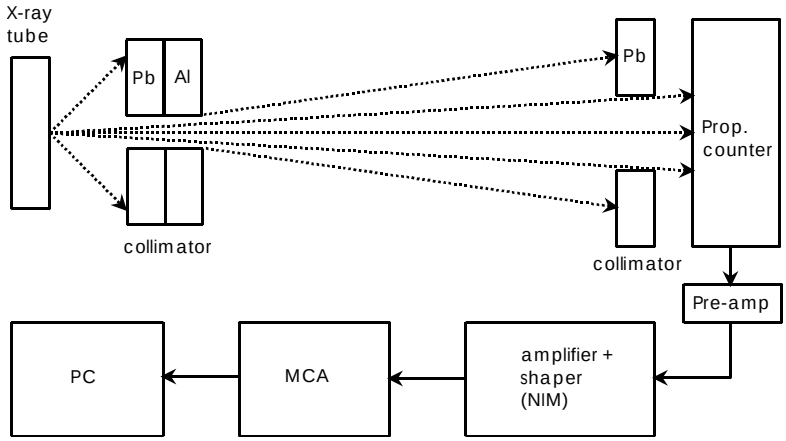

Fig.5.4.2-1. Experimental set up for obtaining spectrum of x-ray tube.

The proportional counter used in the experiment was a cylindrical chamber filled with a gas mixture of 90% argon and 10% methane at atmospheric pressure. A charge sensitive pre-amplifier had been connected very close to the detector for minimum signal loss. Further amplification and shaping of the pulse were done with a standard NIM amplifier and shaper. The spectrum was

taken with a multi-channel analyzer in 1024 channels and the data was then transferred to a PC through a serial port for further processing.

For calibrating the MCA channels, three fluorescence x-ray sources were used: Cu(8.05keV), Rb(13.39keV) and Mo(17.48keV) [Browne and Firestone, 1986]. This choice was made to cover the energy range of the photons emitted by the x-ray tube. A straight line was fitted to the channel-energy curve by least square method,

$$E = 0.0258 \cdot C - 1.2166 \qquad (5.4.2\text{-}1)$$

Here E is the energy of photons and C is the MCA channel number.

To convert the differential count rate with respect to the channel number into differential count rate with respect to energy, it was noted that the integrated counts in both cases should be exactly equal, i.e.,

$$\int \frac{dN}{dC} dC = \int \frac{dN}{dE} dE \qquad (5.4.2\text{-}2)$$

Where dN represents number of photons within channel number C and C+dC or energy E and E+dE.

This relation should hold for any choice of energy and channel number because the coordinate transformation should not change the number of photons. This can only be true if the integrands on right and left hand sides of equation (5.4.2-2) are equal, i.e.,

$$\frac{dN}{dE} = \frac{dN}{dC} \cdot \frac{dC}{dE} \qquad (5.4.2\text{-}3)$$

dC/dE was found by differentiating the straight line fit to be 38.76 channel number per keV.

As with all single-photon-counting detectors, this proportional chamber was also not able to handle high count rates. Therefore the intensity of the x-ray tube had to be decreased by narrow collimators. Two collimators were used for this purpose. One was made with a combination of separate lead and aluminum sheets and had a diameter of 0.8mm. It was placed at 4cm from the focal spot of the x-ray tube. The 8mm thick lead and 1.5mm thick aluminum ensured that the photons would only pass through the hole of the collimator. This collimator was the one which was used for the actual experiments with the beam monitor. Its use with both setups had the advantage that the uncertainties in the size of the collimator hole (and its smoothness) were of no significance for comparing the results. The second collimator was placed at 1.4cm from the entrance window of the proportional counter. This was made by drilling a 6mm diameter hole in a 1.5mm thick lead sheet. The distance between both the collimators was about 165cm. This large distance subtended a very small solid angle at the entrance window of the proportional counter and hence the intensity was decreased to the countable level. Fig.5.4.2-2 shows the spectra of photons absorbed in the proportional counter for different x-ray tube currents. The high voltage of the tube was kept at 25kV during the whole experiment.

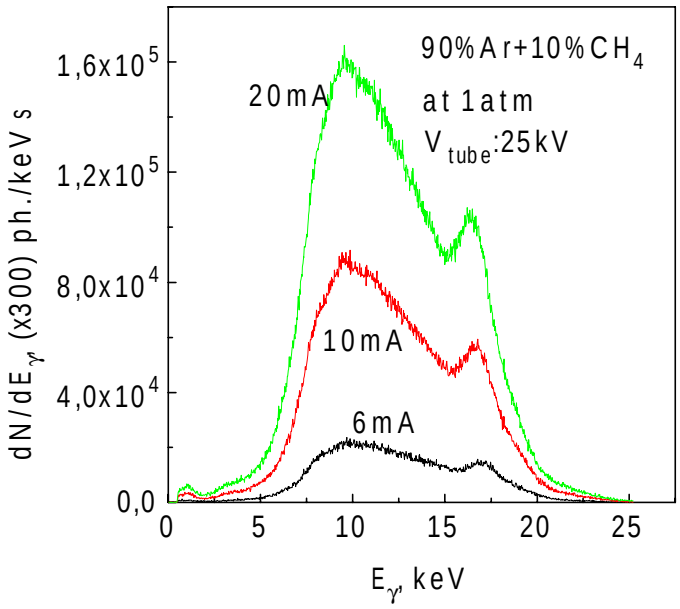

Fig.5.4.2-2. Photon spectra of x-ray tube.

It can be seen in fig.5.4.2-2 that the characteristic Kα line of molybdenum (17.48keV) shifts to the lower energy as the tube current is increased. This is due to the space charge effect in the proportional counter which becomes more and more important at higher intensities. Therefore all the further corrections have been done for the spectrum obtained at 6mA tube current. Below 6mA the x-ray tube was not stable and hence would not had given stable output.

The spectrum of absorbed photons at 6mA tube current after smoothing by adjacent averaging is shown in fig.5.4.2-3.

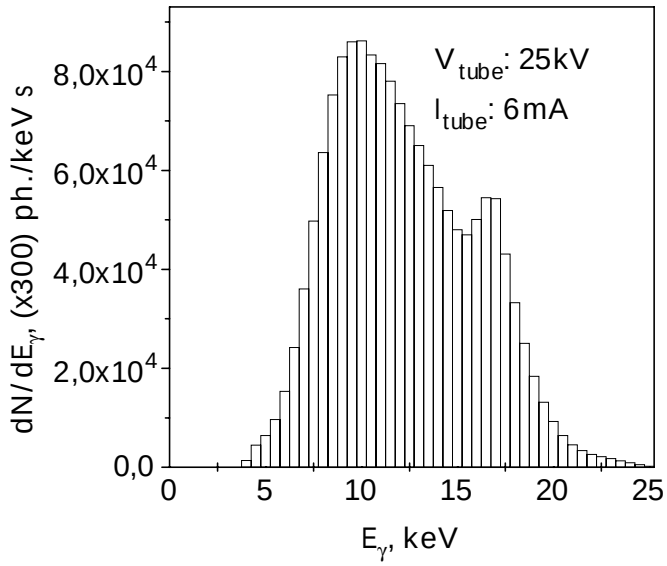

Fig.5.4.2-3. Spectrum of absorbed photons after smoothing by adjacent averaging.

The spectrum shown in fig.5.4.2-3 is the spectrum of photons absorbed in the active volume of the proportional counter. This can be used to derive the spectrum of the incident photons by dividing it by the quantum efficiency of the detector,

$$\left[\frac{dN}{dE}\right]_{inc.} = \frac{\left[\frac{dN}{dE}\right]_{abs.}}{QE(E)} \qquad (5.4.2 - 4)$$

The quantum efficiency is defined as the ratio of number of usefully absorbed photons to the total number of incident photons. For the proportional counter used it is given by,

$$QE(E) = exp(-\mu_{Be} \cdot \rho_{Be} \cdot x_{Be}) \cdot [1 - exp(-\mu_{gas} \cdot \rho_{gas} \cdot x_{gas})] \qquad (5.4.2 - 5)$$

Where μ, ρ and x represent the mass attenuation coefficient, density and thickness of beryllium window and filling gas respectively. Fig.5.4.2-4 shows the spectrum of incident photons obtained in this way.

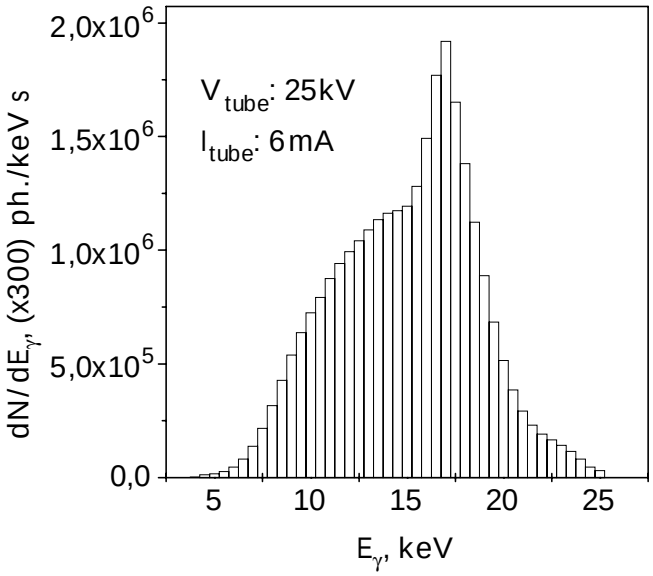

Fig.5.4.2-4. Spectrum of photons incident on the proportional counter.

The spectrum of photons coming out of the collimator placed near the x-ray tube is found by multiplying this spectrum by the fractional solid angle subtended at the window of the detector such that the photons pass through the second collimator. The spectrum shown in fig.5.4.2-5 has been derived after correcting for the fractional solid angle.

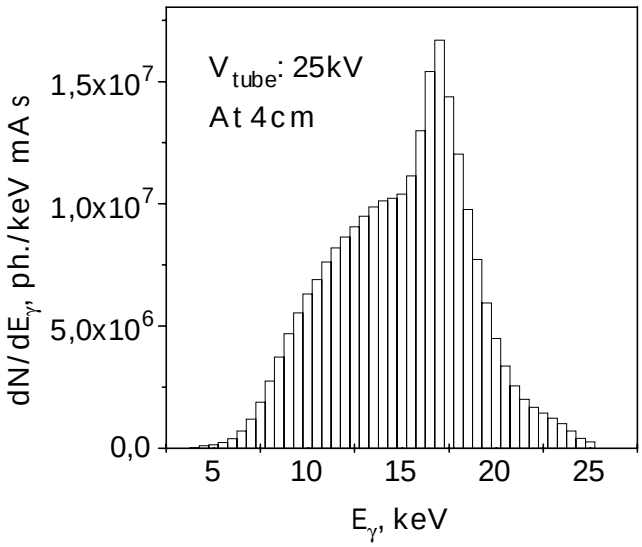

Fig.5.4.2-5. Spectrum of photons coming out of collimator near the x-ray tube.

As mentioned earlier, the collimator near the x-ray tube was the one used in the actual experiments with the beam monitor. This means that no further correction is needed to calculate the spectrum of photons absorbed in the beam monitor. This was done by multiplying the spectrum shown in fig.5.4.2-5 by the quantum efficiency of the beam monitor. The quantum efficiency of the beam monitor is given by (see section 4.1),

$$QE = \exp(-\mu_g \cdot \rho_g \cdot x_{gd}) \cdot \exp(-3\mu_{Al} \cdot \rho_{Al} \cdot x_{Al}) \cdot \exp(-2\mu_{my} \cdot \rho_{my} \cdot x_{my}) \cdot \left(1 - \exp(-\mu_g \cdot \rho_g \cdot x_g)\right) \cdot \left(1 + \exp(-2\mu_{Al} \cdot \rho_{Al} \cdot x_{Al}) \cdot \exp(-\mu_{my} \cdot \rho_{my} \cdot x_{my}) \cdot \exp(-\mu_g \cdot \rho_g \cdot x_g)\right)$$

Here μ is the mass absorption coefficient, ρ is the mass density and x is the thickness of the respective materials characterized by subscripts. Filling gas is represented by g, Aluminum by Al, Mylar by my, and gap of dead region by gd.

Fig.5.4.2-6 shows the spectrum of photons absorbed in the beam monitor.

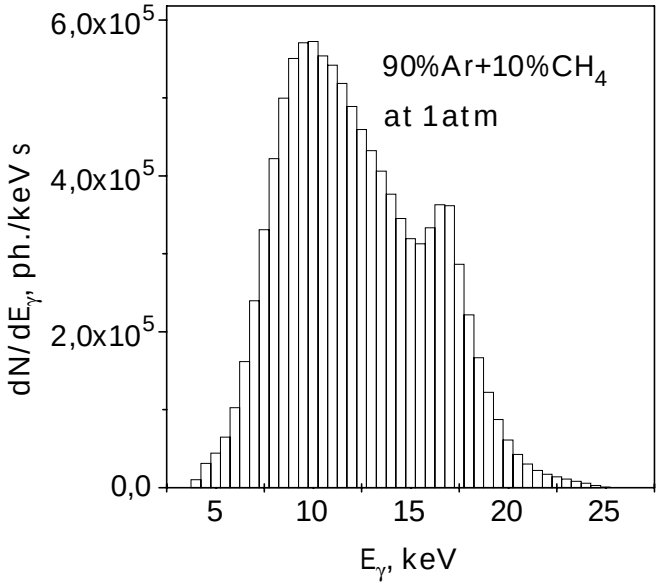

Fig.5.4.2-6. Spectrum of photons absorbed in the beam monitor.

It can be seen that because of the higher probability of photons of lower energy, the average energy of absorbed photons is lower than the average energy of incident photons.

$$< E_{\gamma,inc} >= 15 \ \text{keV}$$
$$< E_{\gamma,abs} >= 12.25 \ \text{keV}$$

The spread in the energy of absorbed photons has been determined by the following relation,

$$\sigma_E^2 = < E_\gamma^2 > - < E_\gamma >^2$$

$$= \frac{\int E_\gamma^2 \cdot \frac{dN_{abs}}{dE_\gamma} \cdot dE_\gamma}{\int \frac{dN_{abs}}{dE_\gamma} \cdot dE_\gamma} - \left[\frac{\int E_\gamma \cdot \frac{dN_{abs}}{dE_\gamma} \cdot dE_\gamma}{\int \frac{dN_{abs}}{dE_\gamma} \cdot dE_\gamma} \right]^2 \qquad (5.4.2\text{-}6)$$

The calculated standard deviation was found to be 3.65keV. This will be used in the next section for the determination of the effective mean energy of absorbed photons in the detector using the actual measurements.

The expected ionization current in the beam monitor can be estimated by the following relation,

$$I_{ion} = \frac{e}{W}\int QE(E)\frac{dN}{dE}dE \qquad (5.4.2-7)$$

Where e is the electronic charge in coulombs, W is the energy needed to produce an electron ion pair in electron volts, and dN/dE represents the number of photons incident per unit time having energy between E and E+dE.

The ionization current measured for 20mA of x-ray tube current was 7.52nA. The expected ionization current calculated from the above relation is 7.94nA. The relative difference between the two values is about 6%. Since there are a number of uncertainties in the corrections carried out to obtain the spectrum of incident photons (e.g. dead time losses had been neglected, error associated with estimation of solid angle etc.) therefore such a difference is not unexpected. Furthermore no recombination losses in the beam monitor were considered giving a larger current as compared to the measured one.

5.4.3. Dependence of the Variance on the Average

The beam monitor developed here is based on the concept of measuring ionization current produced as a result of passage of photons through active volume of the chamber. The current passes through the input stage of the integrator and the corresponding charge is accumulated on an internal capacitor for a certain predefined time. During test measurements the internal capacitor was chosen to be 100pF and the integration time was set to 1mS. The output of the integrator is a voltage signal which depends linearly on the input current through the relation,

$$V_{out} = \frac{I \cdot \tau}{C}$$

Where I is the ionization current, τ the integration time and C the internal capacitance.

The analog voltage is then digitized and the corresponding ADC counts are read by a computer. The linearity of the whole electronics chain ensures that the ADC counts are directly proportional to the ionization current and hence to the energy deposited by photons in the active volume of chamber.

The electronics chain was tested independently and no deviation from linearity was found. However, a direct check of linearity of the whole detection system can not be made unless one uses a very precise and linear source of photons. This lies in the possibility of exactly opposite behavior of photon source and the detector, giving overall a linear response. During recent work the system was tested for linearity with increasing flux of incident x-ray beam and there was no sign of non-linearity up to the achievable intensity of x-rays. However, to discard the possibility of exactly opposite behavior of x-ray tube and detection system, another method was used for linearity test. The concept lies in the Poisson statistics of absorbed photons which ensures that the spread in the energy absorbed in the gas of chamber is directly proportional to the number of incident photons. For a monochromatic beam of photons this means,

$$\sigma^2 = E_\gamma^2 \cdot N_{abs} \qquad (5.4.3\text{-}1)$$

Here N_{abs} is the number of absorbed photons of energy E and σ represents the standard deviation of absorbed energy.

The x-ray tube used during experimentation has, however, a spectrum of energy and intuitively one can think that the variance of the absorbed energy would be larger than that of monochromatic beam because the errors add quadratically. The variance of measurement of absorbed energy in this case can be quantitatively calculated as follows,

$$\sigma_m^2 = \int E_\gamma^2 \cdot \frac{dN}{dE_\gamma} \cdot dE_\gamma \qquad (5.4.3\text{-}2)$$

Here dN/dE_γ is the spectrum of absorbed photons.

The integral represents nothing but the average of the squared energy, i.e.,

$$\sigma_m^2 = < E_\gamma^2 > \cdot N_{abs}$$

If σ_E represents the standard deviation of spectrum of absorbed photons then the following identity holds,

$$\sigma_E^2 = < E_\gamma^2 > - < E_\gamma >^2 \qquad (5.4.3 - 3)$$

Hence

$$\sigma_m^2 = < E_\gamma >^2 \cdot N_{abs} \cdot \left[1 + \frac{\sigma_E^2}{< E_\gamma >^2} \right] \qquad (5.4.3 - 4)$$

As pointed out earlier, the data read by computer is linear with respect to charge deposited on the internal capacitor of the integrator. This in turn means that the above relation can be transformed for the ADC counts with appropriate conversion constants. Hence the variance of the observed counts, considering only Poisson fluctuations, is

$$\sigma_c^2 = \frac{e}{b \cdot C \cdot W} \cdot < N_c > < E_\gamma > \cdot \left[1 + \frac{\sigma_E^2}{< E_\gamma >^2} \right] \qquad (5.4.3 - 5)$$

Here e is the electronic charge in Coulombs, b = 10.17 x 10^{-5} V/count is the conversion factor for ADC counts into analog voltage, C is the integration capacitance in Farads, W is the average energy needed to produce an electron-ion pair in electron volts, and $<N_c>$ is the average of ADC counts.

Apart from Poisson fluctuations, we also have some other additive noise sources in the system, e.g., electronics noise and digitization error. Since the errors add quadratically, therefore the total variance of the measured counts is given by adding the variance of additional noise to the variance only due to Poisson fluctuations,

$$\sigma_c^2 = \sigma_{add}^2 + \frac{e}{b \cdot C \cdot W} \cdot < N_c >< E_\gamma > \cdot \left[1 + \frac{\sigma_E^2}{< E_\gamma >^2} \right] \qquad (5.4.3\text{-}6)$$

This equation implies that, for a linear system, the plot of average counts versus their variance should be a straight line. The y-intercept of this straight line gives the contribution of other noise sources in the system and the slope can be used to determine the effective energy of absorbed photons using,

$$m = \frac{e}{b \cdot C \cdot W} \cdot < E_\gamma > \cdot \left[1 + \frac{\sigma_E^2}{< E_\gamma >^2} \right]$$

The straight line fitted to the measured data is,

$$\sigma_c^2 = \left[(0.29)^2 \pm (0.16)^2 \right] + \left(8.19 \times 10^{-3} \pm 2.17 \times 10^{-4} \right) N_c \qquad (5.4.3\text{-}7)$$

Comparison of this with equation (5.4.3-6) gives the additional noise of 0.29 counts with an error of 0.16 counts. This can be converted into equivalent number of absorbed photons if one knows the effective energy of photons absorbed in the active volume of the detector. The effective energy can be calculated by the slope m of the straight line fit. The slope is a function of the effective energy of absorbed photons and the spread in the spectrum of absorbed photons. This gives a quadratic equation in effective energy of absorbed photons,

$$< E_\gamma >^2 - \frac{mbCW}{e} < E_\gamma > + \sigma_E^2 = 0$$

The spread in the spectrum was calculated in the previous section and was found to be 3.65keV. Using this and the slope of the straight line fit we get the following quadratic equation in terms of effective energy of absorbed photons,

$$< E_\gamma >^2 - (13532.46 \pm 358.17) < E_\gamma > + 13.32 \times 10^6 = 0 \qquad (5.4.3\text{-}8)$$

The solutions to this quadratic equation give,

$$< E_\gamma >= 12.46 \pm 0.21 \text{ keV}$$

The other solution (1.07keV) has been neglected on physical grounds because in the spectrum of incident photons there are no photons of this energy (they are completely absorbed in different materials and air present before the beam monitor). The obtained value of effective energy of absorbed photons (12.46keV) is lower than the average energy of incident photons (15 keV). This can be explained by the higher relative absorption of lower energy photons as compared to higher energy photons in the active volume of the chamber. The average energy of absorbed photons was also calculated from the measured spectrum of absorbed photon. It was found to be 12.25keV giving a relative difference of about 2% as compared to the measured value and lies within the experimental uncertainty. This difference is of course very small and can be attributed to different uncertainties associated with measurement of spectrum of absorbed photons and the following corrections made for making it compatible with the measurements done with the beam monitor (see previous section).

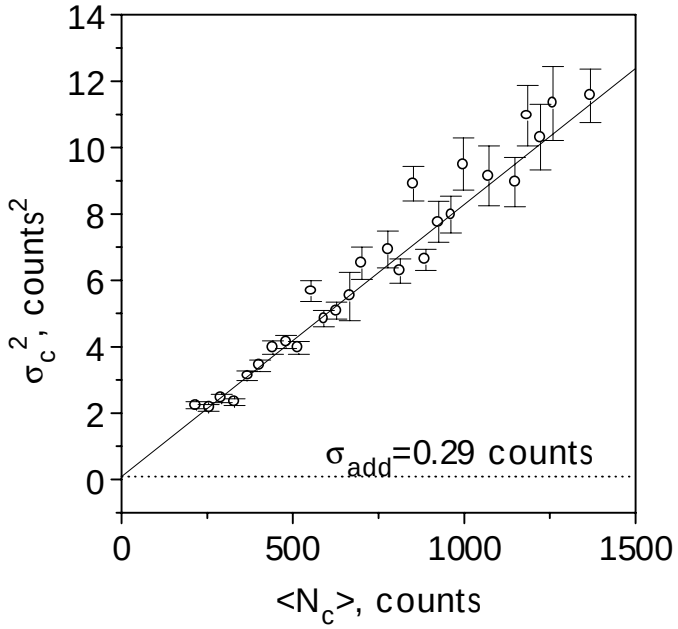

Fig.5.4.3-1. Dependence of variance of counts on respective averages.

Knowing the effective energy of absorbed photons, the measured counts can be converted into number of absorbed photons using the following relation,

$$< N_{\gamma,abs} >= \frac{W}{e \cdot < E_{\gamma,abs} >} \cdot \frac{10.17 \times 10^{-5} \cdot C \cdot < N_c >}{\tau} \qquad \text{photons/s}$$

The variance of counts can be converted into variance of number of absorbed photons by,

$$\sigma^2_{N_{\gamma,abs}} = \left[\frac{W}{e \cdot < E_{\gamma,abs} >} \cdot \frac{10.17 \times 10^{-5} \cdot C}{\tau} \right]^2 \cdot \sigma^2_{N_c} \qquad \text{photons}^2/\text{s}^2$$

Fig.5.4.3-2 shows the behavior of variance of absorbed photons with respect to average number of absorbed photons calculated using the above two relations. It should be noted that the values represent the number of photons absorbed in 1mS integration time.

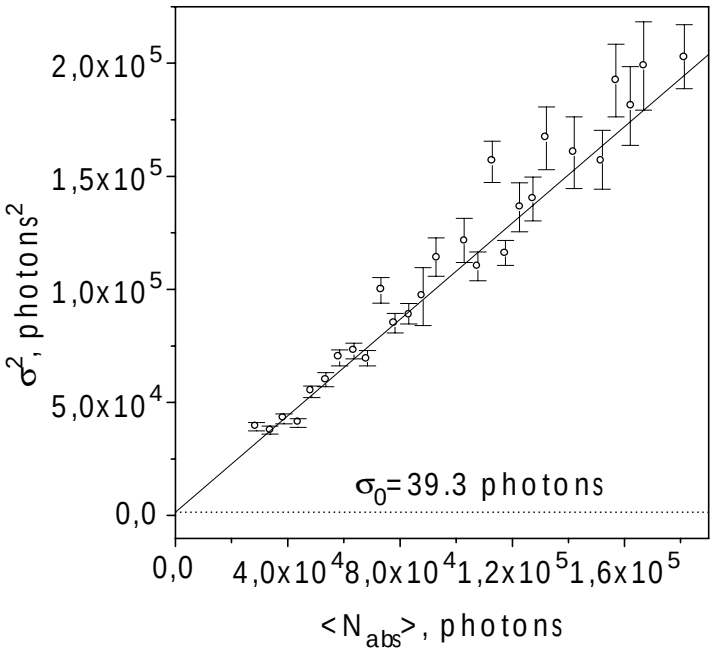

Fig.5.4.3-2. Dependence of number of absorbed photons on the respective averages.

The additional noise of the system as calculated previously from the y-intercept of the straight line fit turned out to be equivalent to 38.4±21.1

photons. The expected electronics noise is, however, equivalent to 35.9 absorbed photons (see section 3.3.3). This of course lies within the experimental uncertainty.

The electronics noise and digitization error of the system were also determined experimentally. For this, the x-ray tube was turned off and digitized data was read in a bunch of 1024 values. The amplification factor at the input stage of the ADC card was increased from 3.33 times to 8 times to detect the noise at all. The resulting distribution is shown in fig.5.4.3-3. The spread in the distribution was found to be equivalent to 64.5 absorbed photons. This value is large as compared to the expected and calculated ones (35.9 and 38.4 respectively). It should be noted that the amplification factor at the input stage of ADC card was increased from 3.33 to 8 which is not very large and therefore it was not proper to detect the small noise in the system. The ADC card had been designed in such a way that this factor could not be increased above this value and therefore the direct determination of the electronics noise could not be done properly. However it should be noted that the method used earlier (straight line fit to the variance-average data) gave the value of the noise very close to the expected one (see sect. 4.4.3).

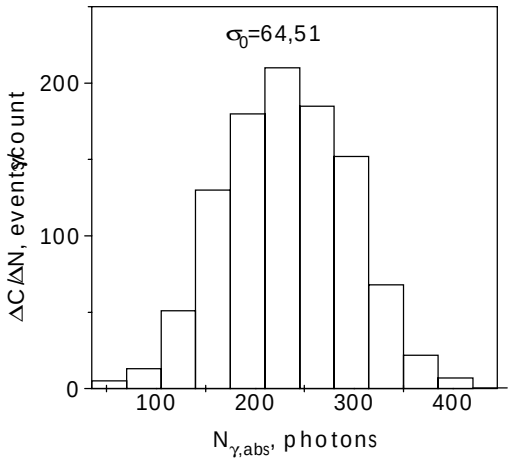

Fig.5.4.3-3. Experimental distribution of dark current in units of absorbed photons.

5.4.4. Accuracy of Measurements

The determination of absolute or relative precision of the system depends heavily on the x-ray source itself which should not have significant drift or ripple to influence the measurements. The x-ray source used so far, however, has some ripple embedded in 100Hz fluctuations and it's harmonics (see section 5.4.1). These fluctuations originate from the electronics of the x-ray tube and can not be directly filtered out. It was found out that the relative amplitude of these fluctuations increases nonlinearly with respect to tube current. Consequently the variance of measurements also increases nonlinearly with increase in x-ray intensity. This in turn means that these fluctuations have to be filtered out if one wants to look at quantum fluctuations in the system. Off line filtration of these fluctuations was carried out through software (see section 5.4.1). It was found out that other noise sources do not contribute significantly to the overall noise. Because of the inherent Poisson noise in the number of absorbed photons, the accuracy of measurement is not a linear function of the measured values even if the electronics noise is constant. The experimental distribution of number of absorbed photons (computed from the ADC counts as outlined earlier in this section) at two different incident x-ray intensities is shown in fig.5.4.4-1.

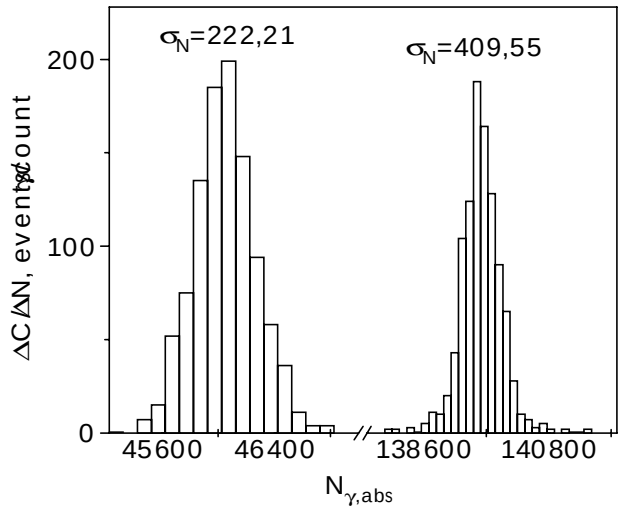

Fig.5.4.4-1 Experimental distribution of absorbed number of photons at two different x-ray intensities.

In order to get more insight into the relative accuracy of measurements with respect to average number of absorbed photons, the relative errors of average of measurements at 95% confidence level have been plotted with respect to average number of absorbed photons, see fig.5.4.4-2. The calculated relative errors only due to Poisson statistics have also been plotted. It is evident that the accuracy of measurement increases with increase in number of absorbed photons. The error in the measured data is at each point larger than the Poisson fluctuation at that point accounting for the electronics noise.

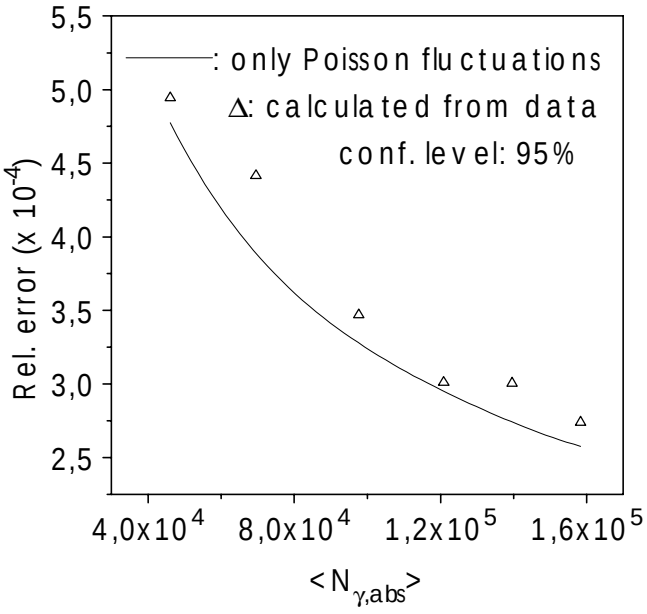

Fig.5.4.4-2. Relative errors in mean number of absorbed photons.

6. Systematic Errors and Stability

There are a number of error sources in a radiation detector which can degrade its performance. Some of these sources pose significant problems only under certain operating conditions (e.g. space charge effect is important at high incident photon intensities) while others contribute (linearly or non-linearly) under all operating conditions. An example of the latter is electronics noise. This has already been discussed in the second chapter and will not be further analyzed here. The effect of space charge, recombination losses and contamination in the detector are discussed briefly in appendices at the end. Here we will look at some of the sources of systematic errors and stability of the system with respect to barometric shifts.

6.1. Effect of Gas Flow

During the experiments with the beam monitor, the flow of filling gas was realized through a bubbler. Bubbler is a special bottle with some fluid in it (for example glycerin). Fig.6.1-1 depicts the schematic of the set up.

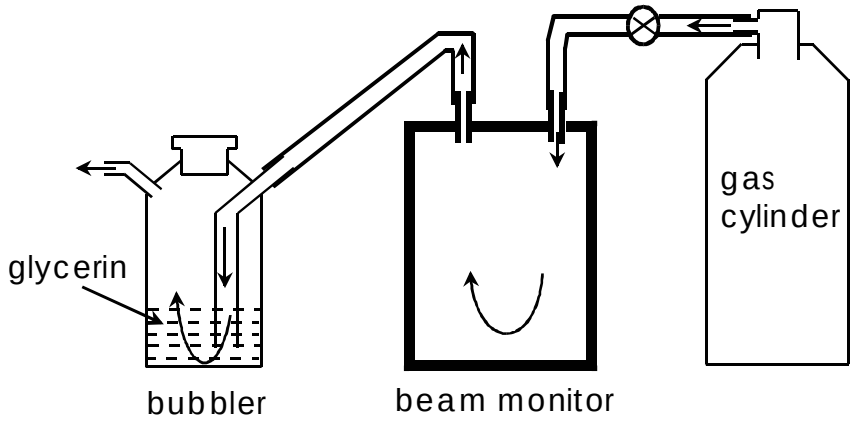

Fig.6.1-1. Schematic of gas flow through beam monitor.

As shown in fig.6.1-1, the bubbler is connected to the outlet of the detector in such a way that the gas has to first flow through the liquid before escaping

out into air. The advantage of letting the gas flow through the liquid is that it does not flow back into the detector. The disadvantage is that a small back pressure is exerted by the liquid above the gas bubble. The amount of pressure exerted by the liquid depends on the height of the liquid above the bubble. As the bubble rises, the pressure decreases and falls to the normal pressure when the bubble escapes the liquid. This rise and fall of pressure continues with the gas flow and its frequency depends on the flow rate of the gas. The back pressure exerted by the liquid is transferred to the chamber of the detector. Since the windows and the electrodes of the chamber are made of very thin (6μm) mylar foil, the length of the active volume inside the chamber changes with the same frequency with which the pressure changes. Fig.6.1-2 shows the normal and changed positions of the electrodes and windows of the beam monitor when the pressure changes by a small amount and produces a change in volume.

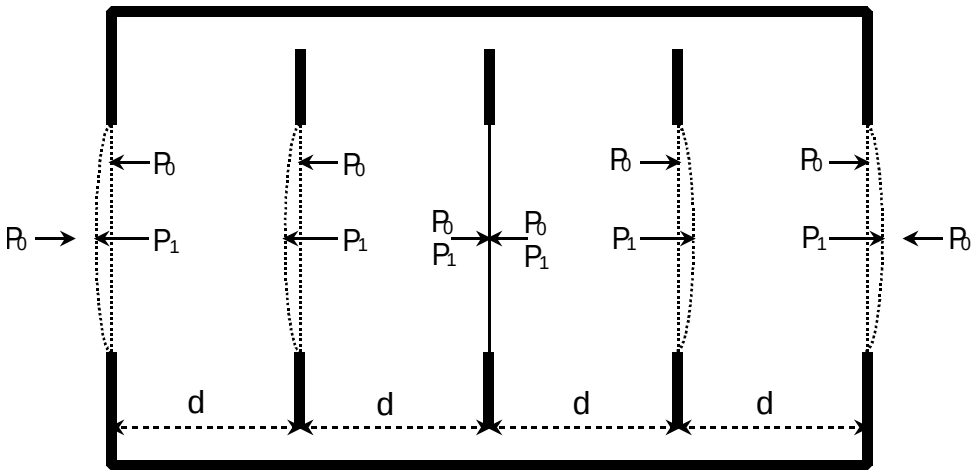

Fig.6.1-2. Change of volume with change in pressure in the beam monitor.

The exactly equal lengths of all the four regions of the beam monitor ensure that the central readout electrode experiences no net force when the pressure changes and therefore retains its shape. The other electrodes and windows, however are bent as the pressure increases and, because of the elastic nature of mylar foil, come back to their normal positions when the

pressure returns to the atmospheric value. Fig.6.1-3 shows an enlarged view of one of the active regions of the chamber.

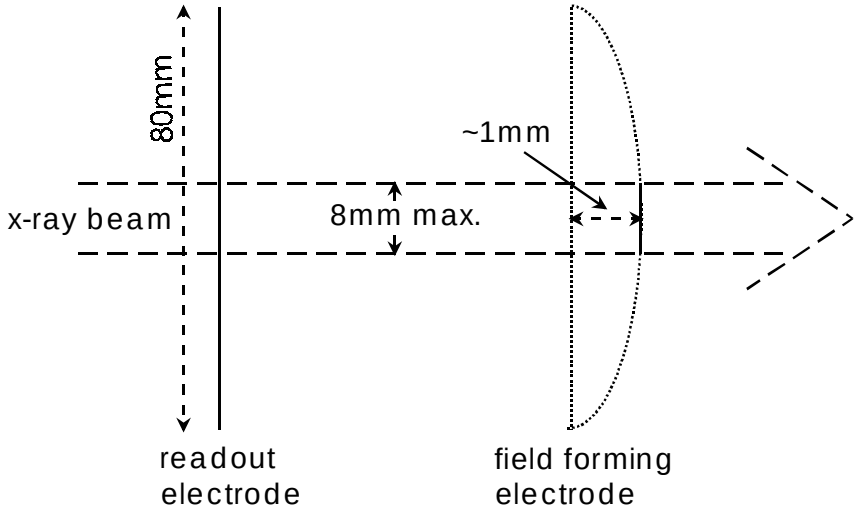

Fig.6.1-3. Exaggerated view of one of the active regions of the beam monitor at normal and increased pressures.

It can be seen in fig.6.1-3 that the expected maximum width of the incident beam of the x-rays is very small as compared to the diameter of the mylar foil on which the electrode has been metalized. Furthermore, during measurements with the beam monitor, the gas flow rate is kept so small that the electrodes and windows experience very small pressure gradients. Such small pressure differences are not expected to push the central part of the foil to more than 1mm. Because of the much larger diameter of the electrode, this change is very nearly equal to the change at the outer edges of the x-ray beam. Hence the change in volume can be described by change in length of the active region.

The increase in the length of the active region takes place relatively slowly because of the low gas flow rate. On the other hand, when the bubble of the gas finally escapes the fluid in the bubbler, the pressure and hence the length of the active region quickly return to their normal values. Mathematically, this can be approximately modeled by the following relations,

$$\left.\begin{aligned} x &= at + d && \text{for} \quad t_0 \le t \le t_1 \\ x &= \frac{at_1}{t_2 - t_1}\left[t_2 - t\right] + d && \text{for} \quad t_1 \le t \le t_2 \end{aligned}\right\} \qquad (6.1\text{-}1)$$

The parameters are explained in fig.6.1-4 which shows a time plot of the change in the length as described above.

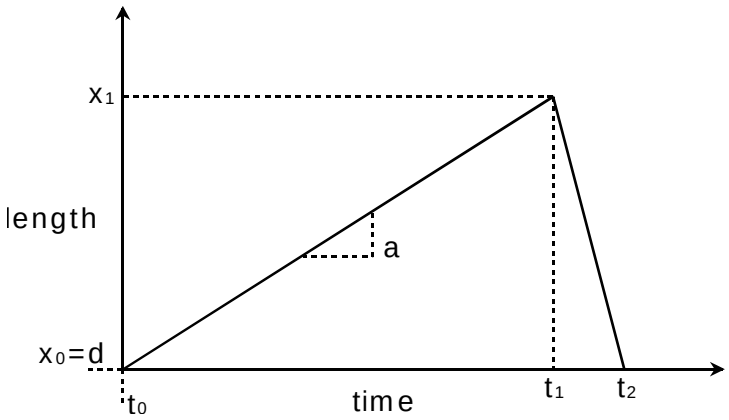

Fig.6.1-4. Modeled time behavior of change in length of active region of beam monitor.

The parameters a, t_1 and t_2 in the above equations depends on the gas flow rate, the density of the fluid in the bubbler and the height of the fluid above the end of the gas inflow pipe in the bubbler. During the measurements with the beam monitor it was observed that for moderate gas flow rates, one whole cycle lasts about one second. In the following we will calculate the effect of gas flow on the ionization current for cycles which last for different times.

For simplicity we take a simple parallel plate ionization chamber with two originally d cm apart electrodes. We assume that one of the electrodes is made of a thick sheet of some metal (e.g. aluminum) which prohibits its expansion or compression in case of pressure change in the chamber. The other electrode is supposed to be made of a very thin mylar foil (of the order of a μm), so that the back pressure exerted by the bubbler on the gas inside the chamber expands the active volume. The reason for assuming one of the electrodes to be fixed is just to make the case compatible with the beam

monitor in which the readout electrode retains its shape even when the pressure changes. We further assume that the chamber is filled with a gas mixture of 90% argon and 10% methane at initially normal pressure.

A change in gas pressure in the chamber does not necessarily mean that the density of the gas changes. There are two other parameters which can change with respect to change in pressure: volume and temperature. If we assume that the thin mylar foils of the electrodes allow the change in volume to such an extent that the density of the gas remains unchanged then the only factor which will affect the ionization current is the change in length of the active volume. The ionization current in the simple parallel plate ionization chamber is given by,

$$I_{ion} = \frac{eN_{\gamma}\left[1 - exp(-\mu\rho x)\right]}{W} \qquad (6.1\text{-}2)$$

Where N_{γ} represents number of photons arriving at the detector per unit time.

The active length x of the chamber can now be assumed to change from its normal value d to some other value d+Δd as a result of change in pressure. The change in length as a function of time is represented by equation 6.1-1. During the first phase (t_0 to t_1 in fig.6.1-4), when the active length increases relatively slowly, the expression for the ionization current (6.1-2) in light of equation 6.1-1 assumes the form,

$$I_{ion}(t) = \frac{eN_{\gamma}\left[1 - exp\{-\mu\rho(at + d)\}\right]}{W} \qquad (6.1\text{-}3)$$

If the measurement of ionization current is repeated every τ second (integration time), then the expected relative change in the ionization current is given by,

$$\frac{\Delta I_{ion}}{I_{ion}} = \frac{exp(-\mu\rho a\tau) - 1}{exp\{\mu\rho(at + d)\} - 1} \qquad (6.1\text{-}4)$$

Similarly, from t_1 to t_2 the ionization current can be calculated by (see equation 6.1-1),

$$I_{ion}(t) = \frac{eN_\gamma\left[1-\exp\left\{-\mu\rho\left(\frac{at_1}{t_2-t_1}[t_2-t]+d\right)\right\}\right]}{W} \qquad (6.1\text{-}4)$$

The relative change in the current in a time τ in this case is,

$$\frac{\Delta I_{ion}}{I_{ion}} = \frac{\exp\left\{\mu\rho\left(\frac{at_1}{t_2-t_1}\tau\right)\right\}-1}{\exp\left\{\mu\rho\left(\frac{at_1}{t_2-t_1}[t_2-t]+d\right)\right\}-1} \qquad (6.1\text{-}5)$$

For numerical analysis of these equations we assume the following parameters,

d = 1cm

Filling gas: 90% argon + 10% methane

Eγ = 10keV

N = 10^9 photons/sec.

t1 = 900 mS

t2 = 1000 mS

a = 0.1 cm/S

τ=1mS

These values have been chosen such that the frequency of barometric shifts caused by the gas flow through bubbler is 1Hz and the maximum change in the length of the active volume is 0.9mm.

Fig.6.1-5 shows the calculated ionization current and the relative error between calculations which are τ second apart. It can be seen that the ionization current behaves almost linearly with respect to change in length of active volume (compare fig.6.1-4). The relative difference between two

consecutive measurements is small when the length is increasing (due to slow change) and is comparatively large when the pressure comes back to its normal value (due to faster change).

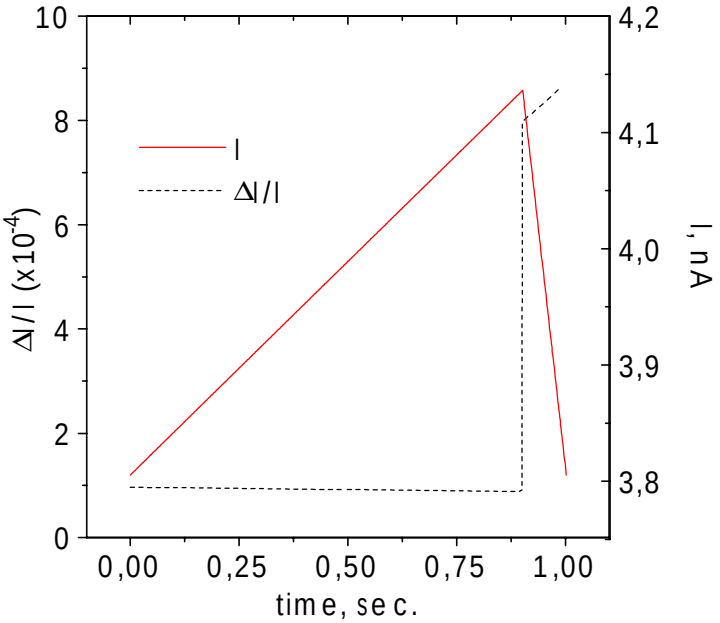

Fig.6.1-5. Calculated ionization current and relative differences between consecutive values.

The relative error in consecutive calculations in this case was found to be of the order of 10^{-4}. In the real situation even if the whole change in length is not exactly linear with respect to pressure change (as we had assumed), it will still be nearly linear at least within the measurement period τ and hence the relative error in the measurement will not be very different from the calculated value. The large difference between the relative errors in the two phases suggest that if the gas flows with larger velocity, the relative errors will be larger. Even at very low gas flow rates, the adverse effect on precision of measurement can not be ignored.

A possible solution to this problem is to use a sophisticated gas system which does not let the gas inside the chamber to be contaminated (e.g. by back flow) and at the same time sustains the pressure to good accuracy. Such a system is, however, very expensive to build and therefore with experiments with the beam monitor another approach was adopted.

First the chamber was flushed with gas using bubbler for more than a day. This freed the inside of the chamber from most of the impurities. The outlet valve of the chamber was then closed and the bubbler was then replaced by a very long gas pipe (~10m) and the gas was flown at a higher velocity. Since the diffusion of the gas takes place slowly, therefore the measurements could be done immediately after without contaminating the chamber.

6.2. Stability

For high precision measurements it is necessary that the detection system is stable with respect to operating conditions such as pressure and temperature. In the course of the experiments small barometric shifts and temperature changes either due to gas flow or environmental conditions are almost always inevitable. Therefore the detection system should have enough stability with respect to these changes to ensure the required precision. In the following we discuss the stability of the developed beam monitor with respect to change in pressure.

The barometric shift could be either caused by temperature change, atmospheric pressure shift or gas flow. If the volume remains constant, the immediate effect of such a shift is the change in gas density. This changes the number of ion pairs being produced and consequently the measured ionization current changes. We will derive an expression for this change in ionization current with respect to change in pressure.

To simplify the computations, we first assume that the pressure change does not significantly affect the change in space charge and recombination. And for the time being we will also assume that the volume remains constant, the effect of volume change with barometric shift has already been discussed in the previous section.

The ionization current caused by the motion of charges produced by the passage of photons is given by,

$$I_{ion} = \frac{e}{W} \cdot \eta \cdot \int QE(E_\gamma, \rho) \cdot E_\gamma \cdot \frac{d\phi(E_\gamma, y, z, t)}{dE_\gamma} dydzdE_\gamma \qquad (6.2\text{-}1)$$

Here we assume that the spectrum dϕ/dE of incident photons does not change during the measurement time. The electronic charge in coulombs is represented by e and W is the energy in electron volts needed to create an ion pair. QE is the quantum efficiency (see section 4.2). η is the collection efficiency which we assume to be constant and ρ denotes the density of the gas. The beam travels in positive x-direction.

If the beam of incident photons is uniform in y and z directions then the above integral can be written as,

$$I_{ion} = \frac{e}{W} \cdot \eta \cdot \int QE(E_\gamma, \rho) \cdot E_\gamma \cdot \frac{d\dot{N}(E_\gamma)}{dE_\gamma} dE_\gamma \qquad (6.2\text{-}2)$$

where,

$$\frac{d\dot{N}(E_\gamma)}{dE_\gamma} = \int \frac{d\phi(E_\gamma, y, z, t)}{dE_\gamma} dydz \qquad \text{and} \qquad \dot{N} = \frac{dN}{dt}$$

Before going forward to calculate the effect due to barometric shifts in the constructed beam monitor, we first look at the special case of a simple parallel plate ionization chamber in a mono-energetic beam of incident photons.

For a mono-energetic beam, equation (6.2-2) assumes the form,

$$I_{ion} = \frac{e}{W} \cdot \eta \cdot \dot{N} \cdot E_\gamma \cdot QE(\rho) \qquad (6.2\text{-}3)$$

A parallel plate geometry in which the photons pass through the electrodes (distance d apart), the absorption efficiency (QE) is given by,

$$QE(\rho) = 1 - exp\left(-\mu_g \cdot \rho \cdot d\right) \qquad (6.2 - 4)$$

If we assume that the volume and the temperature do not change with change in pressure, then according to the general gas law (PV/T = constant), the density will depend linearly on the pressure, i.e.,

$$\rho(P) = \frac{P}{P_O} \cdot \rho(P_O) \qquad (6.2 - 5)$$

In this case, the equation (6.2-3) becomes,

$$I_{ion} = \frac{e}{W} \cdot \eta \cdot \dot{N} \cdot E_\gamma \cdot \left[1 - exp\left(-\mu_g \cdot \frac{P}{P_O} \cdot \rho_O \cdot d\right)\right] \qquad (6.2 - 6)$$

Here $P\text{-}P_0$ is the change in pressure and ρ_0 is the density of gas at pressure P_0.

The rate of change of current with respect to pressure can be calculated by differentiating the above equation with respect to pressure P,

$$\frac{\partial I_{on}}{\partial P} = \frac{e}{W} \cdot \eta \cdot \dot{N} \cdot E_\gamma \cdot \mu_g \cdot \frac{\rho_O}{P_O} \cdot d \cdot exp\left(-\mu_g \cdot \frac{P}{P_O} \cdot \rho_O \cdot d\right) \qquad (6.2 - 7)$$

If the changes are not very large, we can also write the above equation in the following form,

$$\Delta I_{on} = \frac{e}{W} \cdot \eta \cdot \dot{N} \cdot E_\gamma \cdot \mu_g \cdot \frac{\rho_O}{P_O} \cdot d \cdot exp\left[-\mu_g \cdot \left(1 + \frac{\Delta P}{P_O}\right) \cdot \rho_O \cdot d\right] \cdot \Delta P \qquad (6.2 - 8)$$

Where $\Delta P = P\text{-}P_0$.

This equation shows that the absolute change in ionization current depends linearly on the total integrated photon flux N (photons/second). However its dependence on energy is not linear because the mass attenuation coefficient μ is energy dependent.

The relative change in ionization current can be calculated using equations (6.2-6) and (6.2-8),

$$\frac{\Delta I_{ion}}{I_{ion}} = \frac{\mu_g \cdot \frac{\rho_0}{P_0} \cdot d \cdot \exp\left[-\mu_g \cdot \left(1+\frac{\Delta P}{P_0}\right) \cdot \rho_0 \cdot d\right] \cdot \Delta P}{\left[1-\exp\left\{-\mu_g \cdot \left(1+\frac{\Delta P}{P_0}\right) \cdot \rho_0 \cdot d\right\}\right]} \qquad (6.2-9)$$

The relative change in ionization current is independent of number of incident photons. The dependence on other parameters is complex and will now be numerically investigated. We take argon as the filling gas in a parallel plate ionization chamber with electrode separation of 1cm. Fig.6.2-1 shows the computed behavior of relative change in ionization current at different incident photon energies.

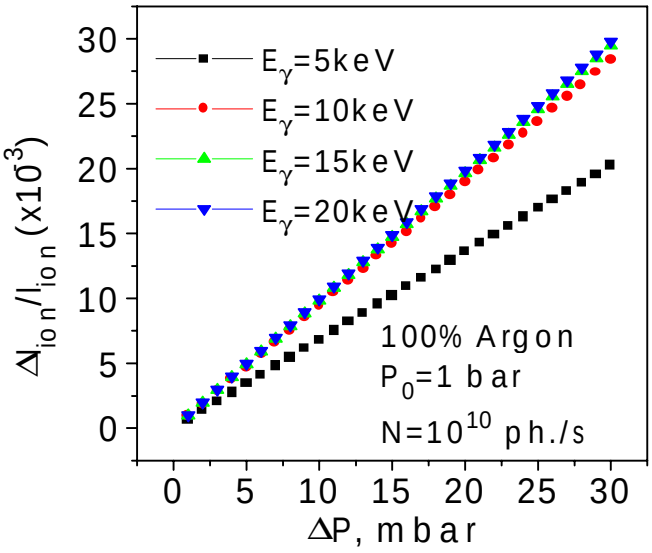

Fig.6.2-1. Dependence of relative change in ionization current on the change in pressure.

It is evident from fig.6.2-1 that the relative change in ionization current increases with increasing incident photon energy. However, the dependence is not strong at energies above 10keV. At lower energies (around 5keV) the abrupt increase in mass absorption coefficient of the gas is responsible for higher ionization current and lower relative change in ionization current.

The absolute change in ionization current at different incident photon energies with a flux of 10^{10} photons/second was calculated using equation (6.2-8). For simplicity it was assumed that all produced charges are collected, i.e., $\eta=1$. The computed behavior is shown in fig.6.2-2.

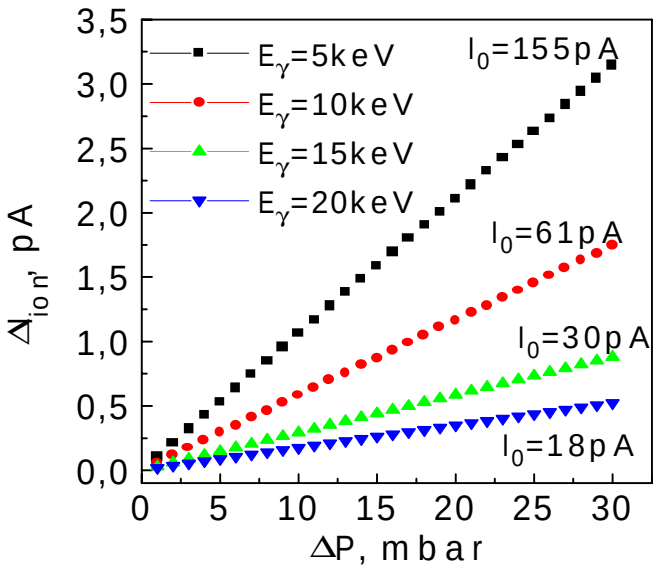

Fig.6.2-2. Dependence of absolute change in ionization current on change in pressure with N=10^{10} photons/s and $\eta=1$.

Up till now we have considered that the system was operating initially at normal pressure (1bar) and the barometric shifts were small (in mbar). The reason for this assumption were the thin mylar windows which can not withstand large pressure gradients. Now we try to see what happens when the operating pressure is different from the normal pressure and a sudden large change in pressure occurs. Of course in this case the change in ionization current will be large but the computations at different initial pressure values could give an idea of the relative stability of the system. For the same case of previous computations we get the behavior of abrupt large change in pressure by using equation (6.2-9). Fig.6.2-3 shows the plotted behavior. It can be seen that the higher the pressure the more stable is the system. This means that if the mechanical design of the detector permits, it is desirable to operate the system at a higher pressure. This, of course, was not

possible for the constructed beam monitor and therefore during the test measurements the system was operated at normal pressure.

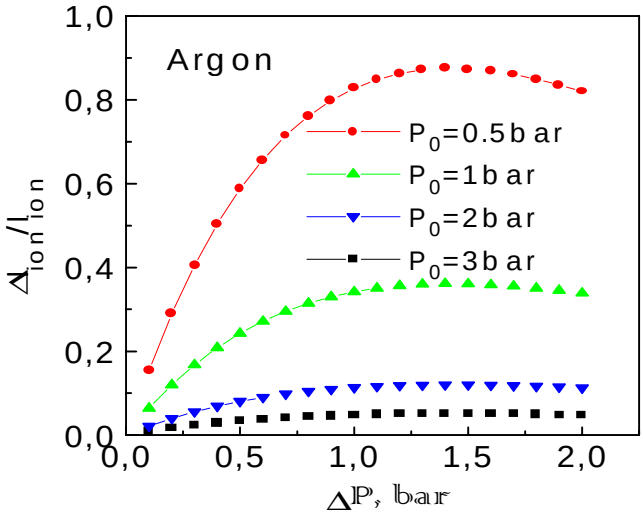

Fig.6.2-3. Effect of change in pressure on relative change in ionization current at different initially applied pressures.

Now we look at the case of the beam monitor. The quantum efficiency of the system is given by,

$$QE = \exp\left(-\mu_g \cdot \frac{P}{P_O} \cdot \rho_g \cdot x_{gd}\right) \cdot \exp(-3\mu_{Al} \cdot \rho_{Al} \cdot x_{Al}) \cdot \exp(-2\mu_{my} \cdot \rho_{my} \cdot x_{my}) \cdot \left[1 - \exp\left(-\mu_g \cdot \frac{P}{P_O} \cdot \rho_g \cdot x_g\right)\right] \cdot \left[1 + \exp(-2\mu_{Al} \cdot \rho_{Al} \cdot x_{Al}) \cdot \exp(-\mu_{my} \cdot \rho_{my} \cdot x_{my}) \cdot \exp\left(-\mu_g \cdot \frac{P}{P_O} \cdot \rho_g \cdot x_g\right)\right] \quad (6.2\text{-}10)$$

Here we have again used the same assumption that the volume and temperature remain constant and so the density of the gas depends linearly on the pressure.

Equation (6.2-2) gives the measured ionization current when integrated (in width of the beam) photon flux with energy spectrum of dN/dE is incident on a detector with quantum efficiency QE.

$$I_{ion} = \frac{e}{W} \cdot \eta \cdot \int QE(E_\gamma, \rho) \cdot E_\gamma \cdot \frac{d\dot{N}(E_\gamma)}{dE_\gamma} dE_\gamma \qquad (6.2-2)$$

The change in ionization current with change in pressure is obtained by differentiating both sides with respect to pressure P,

$$\frac{\partial I_{ion}}{\partial P} = \frac{e}{W} \cdot \eta \cdot \int \frac{\partial QE(E_\gamma, \rho)}{\partial P} \cdot E_\gamma \cdot \frac{d\dot{N}(E_\gamma)}{dE_\gamma} dE_\gamma \qquad (6.2-11)$$

Differentiating QE with respect to pressure gives,

$$\frac{\partial QE}{\partial P} = C_1^3 \cdot C_2^2 \cdot \mu_g \cdot \frac{\rho_{gO}}{P_O} \cdot x_g \cdot \exp\left(-\mu_g \cdot \frac{P}{P_O} \cdot \rho_g \cdot x_{gd}\right) \cdot \left[\exp\left(-\mu_g \cdot \frac{P}{P_O} \cdot \rho_g \cdot x_{gd}\right) \cdot \left\{2 - 2C_1^2 \cdot C_2 + 3C_1^2 \cdot C_2 \cdot \exp\left(-\mu_g \cdot \frac{P}{P_O} \cdot \rho_g \cdot x_{gd}\right)\right\} - 1\right] \qquad (6.2\text{-}12)$$

Where,

$$C_1 = \exp(-\mu_{Al} \cdot \rho_{Al} \cdot x_{Al}) \quad \text{and}$$
$$C_2 = \exp(-\mu_{my} \cdot \rho_{my} \cdot x_{my}) \cdot$$

Using the identity $P=P_0+\Delta P$ and the above differential, equation (6.2-12) can be written in the computationally convenient form as,

$$\Delta I_{ion} = \frac{e}{W} \eta \Delta P \int C_1^3 C_2^2 \mu_g \frac{\rho_{gO}}{P_O} x_g \exp\left\{-\mu_g \left(1 + \frac{\Delta P}{P_O}\right) \rho_g x_{gd}\right\} \cdot \left[\exp\left(-\mu_g \left(1 + \frac{\Delta P}{P_O}\right) \rho_g x_{gd}\right) \cdot \left\{2 - 2C_1^2 C_2 + 3C_1^2 C_2 \exp\left(-\mu_g \left(1 + \frac{\Delta P}{P_O}\right) \rho_g x_{gd}\right)\right\} - 1\right] \cdot E_\gamma \frac{d\dot{N}(E_\gamma)}{dE_\gamma} dE_\gamma \qquad (6.2-13)$$

Ratio of equation (6.2-13) to equation (6.2-2) gives the relative change in ionization current with change in pressure.

Since we have already measured the spectrum of incident photons emanating from the x-ray tube used in experiments with the beam monitor (see chapter 4), we can use equations (6.2-13) and (6.2-2) to compute the relative change in ionization current with increase or decrease in pressure within the chamber volume.

Fig.6.2-4 shows the relative change in ionization current corresponding to increase in pressure in chamber volume. It is evident that the behavior of the beam monitor with small changes is linear with respect to small barometric shifts.

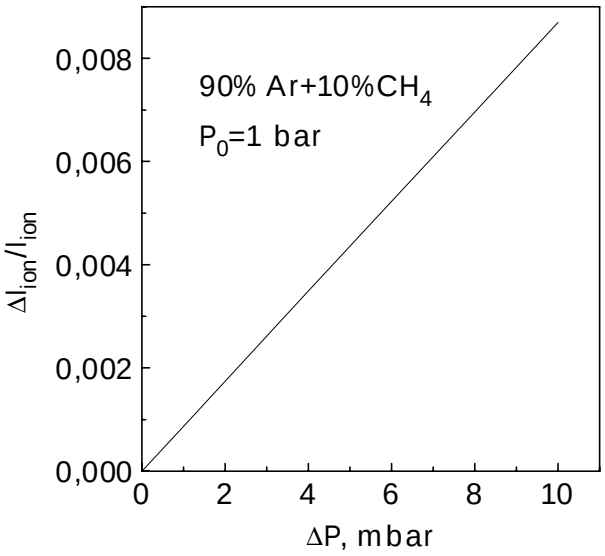

Fig.6.2-4 Relative change in ionization current with change in pressure in chamber volume.

Fig.6.2-4 shows that the barometric shifts of even several millibars is enough to deteriorate the precision of measurement to unacceptable levels. It should however be noted that in the following calculations it was assumed that the active volume of the monitor does not change with change in pressure. This is not absolutely true since the thin mylar foil used to construct the windows and the electrodes can not withstand pressure gradients. In actual practice the

pressure change is almost always followed by change in active volume except when the barometric shift is very small (less than a mbar). The effect of the change in volume with change in pressure has already been discussed in section 6.1.

7. Conclusions

The goal of this project was to build a high precision beam intensity monitor for synchrotron radiation which works at the limit of quantum fluctuations. The system has been successfully built and the test measurements show that the required precision of better than 10^{-4} has been achieved. Furthermore it could be shown that the system works at the limit of quantum noise according to the anticipation. In the following we review some of the important features of the detector and results of the test measurements.

- The constructed beam monitor works as an ionization chamber in integration mode. It showed ionization chamber plateaus having slopes of less than 2% per 1000 volts when a gas mixture of 90% argon and 10% methane was used. With the gas mixture of argon and carbon dioxide, the plateaus had larger slopes (>3% per 1000 volts). This is understandable on physical grounds since carbon dioxide has large electron capture cross section and consequently larger recombination probability (see Appendix-D) as compared to that of methane. In all other experiments methane was used as the admixture of argon. The advantage of using methane is that the net attenuation of incident photon beam can be controlled by changing concentration of methane. In fact the concentration of argon can essentially go to zero and the system can be operated only with methane (this might be desirable at low energies, around 5keV) since the attenuation cross section of argon at low energies is very high (see section 4.1 for detailed description).
- A high precision system should also behave linearly with respect to incident photon intensity. The linearity of the system was checked with a powerful x-ray tube. The intensity of photons was changed by x-ray tube current. No deviation from linearity was observed up to the achievable intensity of x-rays (see section 4.3.2). It should, however, be pointed out that at high photon fluxes (>10^{11} photons/s) the space charge effect becomes significant (see Appendix-A). As a consequence, the electric

field inside the active volume of the chamber changes and does not remain uniform throughout the active length. This affects the electron and ion drift velocities and the recombination losses increase. The charges are therefore not properly collected and this loss of information appears as non-linearity in the system with respect to incident photon flux. In order to at least minimize this effect, the active length of the beam monitor has been kept small (but larger than the threshold, see chapter 2) such that at even high photon flux the electric field at the edges is not decreased so much that the recombination losses become significant.

- By taking Fourier transform of the measured data it was observed that the data contained fluctuations at 100 Hz and its harmonics. This was later found to originate from the electronics of the x-ray setup. Since these fluctuations could not be filtered by hardware therefore off line software filtration of the measured data was performed using a band stop filter in frequency space. This was necessary to study the inherently imbedded quantum fluctuations in the data.
- In order to calibrate the beam monitor and to obtain the spread in the spectrum of absorbed photons (to be used for calculating the effective energy of absorbed photons from the measured data), the spectrum of photons coming out of the x-ray tube was measured. For this a proportional counter was used. The spread in the spectrum of absorbed photons was found to be 3.65keV (see section 5.4.2).
- The variances of measurements was found to depend linearly on the respective averages (see section 5.4.3). This shows that the system works at the limit of quantum noise. In other words, the fluctuations other than Poisson spread in the data were very small and remained nearly constant with respect to intensity of incident photons. This is a basic criteria of high precision systems.
- The electronics noise obtained from the straight line fit of variance-average data was found to contain large error (0.22±0.16 counts) but the value was very close to the expected noise obtained from the data sheets provided by the manufacturer of the integrator and ADC chips. In any

case, the electronics noise was found to be constant with respect to ionization current and therefore poses no problems for precision of measurements at high incident photon intensities.

- The relative precision of intensity measurement was found to be approaching the desired value of 10^{-4} with increase in the number of incident photons. It is therefore expected that the beam monitor will show even better performance with synchrotron radiation where the incident photon flux is higher than 10^9 per second.
- For high precision measurements at a synchrotron facility it is necessary that the gas system of the beam monitor be properly prepared such that no pressure gradients occur during the operation. The monitor is highly susceptible to the barometric shifts. Use of bubbler is not recommended because it exerts some back pressure and consequently the active length of the chamber fluctuates.

APPENDIX-A

Space Charge Effect

The positive ions produced in the active volume of the chamber drift and diffuse slowly towards the negative electrode. Because of their slower velocity as compared to electrons (roughly 1000 times slower), they are accumulated in the active volume of the chamber. This space charge produces an electric field opposite to that of originally applied one and thus the net electric field experienced by electrons and ions is reduced. Consequently the drift properties change and hence the ionization current measured by the connected circuitry changes. Although such space charge effects are not very significant in ionization chambers operated at normal pressure, nevertheless to get more exact information about the developed system, the following calculations were performed.

First we consider the active volume of the chamber to consist of a parallel plate capacitor with gap d as shown in fig.A-1. The photon beam passes through the electrodes perpendicularly and produces electron-ion pairs in the filling gas.

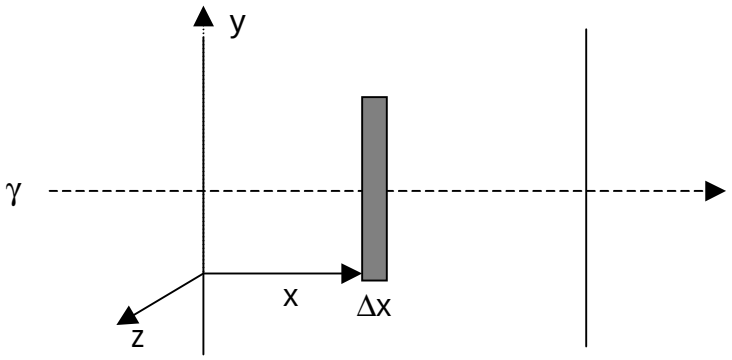

Fig.A-1. Schematic for calculation of space charge.

The equations of motion of positive ions in an electric field E are,

$$\left.\begin{aligned} &\nabla \cdot \vec{E} = \frac{\rho_+}{\varepsilon}; \\ &\overrightarrow{J_+} = \rho_+ \overrightarrow{v_+}; \\ &\nabla \cdot \overrightarrow{J_+} = O; \\ &\overrightarrow{v_+} = \mu_+ \vec{E}; \end{aligned}\right\} \qquad \text{(A-1)}$$

Here ρ_+ is the density of positive ions moving with velocity v_+ and mobility μ_+. The current density of ions is represented by J_+. ε is the dielectric constant of the gas.

The above relations immediately imply that,

$$\nabla \cdot \left[\vec{E}\left(\nabla \cdot \vec{E}\right)\right] = O \qquad \text{(A-2)}$$

To simplify the calculations we assume our detector to be composed of two infinite parallel plates. This assumption is valid, since the diameter of the electrodes is much larger than the distance between them and the electric field lines have been made parallel with the help of field rings and so the charges do not experience any distorted edge fields. With this assumption, we now have to solve the above equation in just one dimension. In this case it

$$\frac{d}{dx}\left[E\left(\frac{dE}{dx}\right)\right] = O$$

The integration of this yields,

$$E = \left[2\left(C_1 x + C_2\right)\right]^{1/2} \qquad \text{(A-3)}$$

The C_1 and C_2 are constants of integration to be determined from the initial conditions as follows.

We have to determine the value of electric field at the boundaries of the active volume, i.e., at x=0 and d. If the electrode at x=0 is at negative

potential with respect to that at x=d then we have the following initial conditions.

$$E = -\frac{U_O}{d} - E_+ \qquad at\ x = O$$

$$E = \frac{U_O}{d} - E_+ \qquad at\ x = d$$

Where E_+ is the electric field contribution of the space charge due to accumulation of positive ions in the active volume of the chamber. U_0 is the potential difference applied to the electrodes.

Therefore, the initial conditions at x=0 and x=d give,

$$C_1 = -2 \cdot \frac{U_O \cdot E_+}{d^2}$$

$$C_2 = \frac{1}{2}\left(\frac{U_O}{d} + E_+\right)^2$$

With these two constants, the expression for net electric field intensity at any point x becomes,

$$E = \left[-4 \cdot \frac{U_O \cdot E_+}{d^2} \cdot x + \left(\frac{U_O}{d} + E_+\right)^2\right]^{1/2} \qquad \text{(A - 4)}$$

The electric field intensity E_+ due to space charge can be computed using the Gauss's law for electrostatic fields applied to an infinitesimal length dx and then summing over the whole length of the active volume. Because of the exponential law of photon absorption and the preferred motion of positive ions in the direction of the net electric field, the space charge density is not uniform throughout the active volume. And hence the Gauss's law can not be directly applied to the whole volume without considering this non-uniformity. But the charge density in a small volume element can be considered uniform and the Gauss's law can be applied to this element. The

sum over all these elements will give the net field at the end points of the active volume.

We consider a small element Δx at a distance x from the negative electrode (see fig.5.1-1). The number of photons absorbed at a distance x' from x=x in Δx is given by the exponential law,

$$\phi_{abs} = \phi_O(y,z,t) \cdot exp(-\mu \cdot \rho \cdot x) \cdot [1 - exp(-\mu \cdot \rho \cdot x')] \qquad (A-5)$$

Here ϕ_0 is the incident photon flux at x=0, μ is the mass absorption coefficient of photons in the gas used and ρ is the gas density.

If the photon flux is constant during the integration time of ionization current, then the amount of space charge in the volume element being considered is given by,

$$Q = \frac{e \cdot E_\gamma}{W \cdot v_+} \cdot exp(-\mu \cdot \rho \cdot x) \cdot \int_{y=O}^{h} \int_{z=O}^{b} \phi_O(y,z,t) dy dz \cdot \int_{x'=x}^{x+\Delta x} [1 - exp(-\mu \cdot \rho \cdot x')] dx' \qquad (A-6)$$

Here W is the energy needed by photons of energy E_γ to create an ion pair, e is the electronic charge in coulombs, and v_+ is the drift velocity of positive ions.

Upon integration we get the space charge in the volume element $hb\Delta x$,

$$Q = \frac{e \cdot E_\gamma \cdot N_O}{W \cdot v_+} \cdot exp(-\mu \cdot \rho \cdot x) \cdot \left[\Delta x - \frac{exp(-\mu \cdot \rho \cdot x)}{\mu} \cdot \{1 - exp(-\mu \cdot \rho \cdot \Delta x)\} \right] \qquad (A-7)$$

where

$$N_O = \int_{y=O}^{h} \int_{z=O}^{b} \phi_O(y,z,t) dy dz \cdot$$

If the mean free path of photons λ (=$1/\mu\rho$) is very large as compared to elemental length Δx then the above identity reduces to,

$$Q = \frac{e \cdot E_\gamma \cdot N_O}{W \cdot v_+} \cdot exp(-\mu \cdot \rho \cdot x) \cdot \Delta x \cdot \left[1 - exp(-\mu \cdot \rho \cdot x)\right] \qquad \text{(A - 8)}$$

Now we can calculate the electric field intensity due to this charge using Gauss's law which states that the net electric field intensity from a closed surface is derivable from the amount of charge enclosed by that surface according to,

$$\oint \vec{E} \cdot \vec{n} ds = \frac{Q}{\varepsilon}$$

Since the volume element we have chosen is of infinitesimal length Δx therefore only the x-component of the electric field intensity is of significance here.

Hence,

$$E_{\Delta x} \cdot \int_{y=O}^{h'} \int_{z=O}^{b'} dydz = \frac{e \cdot E_\gamma \cdot N_O}{2 \cdot \varepsilon \cdot W \cdot v_+} \cdot exp(-\mu \cdot \rho \cdot x) \cdot \Delta x \cdot \left[1 - exp(-\mu \cdot \rho \cdot x)\right] \qquad \text{(A - 9)}$$

Here the factor 2 comes from integrating the right and left surfaces and h' and b' are the height and breadth of the surface out of which the electric field lines are emanating. Their values are determined by taking into account the photon beam area and the mean transverse spread of ions during integration time.

The electric field intensity from the volume element being considered is then given by,

$$E_{\Delta x} = \frac{e \cdot E_\gamma \cdot N_O}{2 \cdot \varepsilon \cdot W \cdot v_+ \cdot h' \cdot b'} \cdot exp(-\mu \cdot \rho \cdot x) \cdot \Delta x \cdot \left[1 - exp(-\mu \cdot \rho \cdot x)\right] \qquad \text{(A - 10)}$$

The net electric field at the edges of the volume enclosed by the electrodes is of course the sum over all elements of length Δx, i.e.,

$$E_+ = \frac{e \cdot E_\gamma \cdot N_O}{2 \cdot \varepsilon \cdot W \cdot v_+ \cdot h' \cdot b'} \cdot \int_{x=O}^{d} exp(-\mu \cdot \rho \cdot x) \cdot [1 - exp(-\mu \cdot \rho \cdot x)] \cdot dx$$

This gives,

$$E_+ = \frac{e \cdot E_\gamma \cdot N_O}{4 \cdot \varepsilon \cdot W \cdot v_+ \cdot h' \cdot b' \cdot \mu \cdot \rho} \cdot [1 + exp(-2 \cdot \mu \cdot \rho \cdot d) - 2 \cdot exp(-\mu \cdot \rho \cdot d)] \qquad (A-11)$$

Hence with the help of equation (A-4) and the above relation, the net electric field intensity as a function of distance x from negative electrode can be calculated.

It can be seen from the above relation that the electric field intensity due to space charge depends linearly on the number of incident photons per unit time and inversely on the drift velocity of positive ions. The linear dependence on incident number of photons implies that at high rates the effect of space charge might not be insignificant. In the following we estimate this dependence for the chamber developed and the filling gas used.

The mobility of different ions in different gases have been experimentally determined [Sauli 1977]. In usual units ($cm^2/V.S$), the mobility of Ar^+ in argon is 1.7 and that of CH_4^+ in argon is 1.87. Since the concentration of methane is very small (10%) as compared to that of argon therefore we can use this value to estimate the mean value of mobility using the Blank rule,

$$\frac{1}{\mu_+} = \sum_i \frac{a_i}{\mu_i}$$

Here a_i are the partial concentrations in the mixture.

This gives for the mixture of 90% argon and 10% methane in standard conditions,

$$\mu_+ = 1.72 \quad cm^2 / V \cdot S$$

The drift velocity of positive ions depends linearly on the applied electric field, the mobility being the proportionality constant. For the applied potential of 100 volts applied at electrodes 0.8 cm apart we get the drift velocity of 430cm/S.

The parameters h' and b' can be calculated by considering the mean square displacement of positive ions in y and z directions,

$$\left.\begin{aligned} h' &= h + 2\cdot\sqrt{\overline{y^2}} = h + 2\cdot\sqrt{6\cdot D\cdot\tau} \\ b' &= b + 2\cdot\sqrt{\overline{z^2}} = b + 2\cdot\sqrt{6\cdot D\cdot\tau} \end{aligned}\right\} \qquad \text{(A-12)}$$

Here h and b are the height and breadth of incident photon beam, D is the diffusion coefficient of positive ions in the gas mixture and τ is the integration time. The justification of this approximation is that since there is no transverse electric field therefore the transverse movement of positive ions is completely determined by diffusion coefficient D.

For our case we get h'=h+0.03 cm and b'=b+0.03 cm for 1mS integration time. Here we have used the diffusion coefficient of only argon molecule since that of methane could not be found in the literature. This is of course not a very good approximation because the ionization energy of methane is less than that of argon and as a consequence of charge exchange between molecules the main carrier of charges are methane molecules. Still the non-availability of the value of diffusion coefficient of methane in the used gas mixture forced to use the value for argon in order to get at least an order of magnitude estimate of the space charge effect.

If we take the incident beam dimensions to be 4X8 mm^2, together with the parameters we have just calculated, we get the expression for electric field intensity as a function of incident number of 10keV photons,

$$E_+ = 4.4\times 10^{-10}\cdot N_0$$

The net electric field as a function of distance x from first electrode is calculated by equation (A-4),

$$E = \left[-4 \cdot \frac{U_O \cdot 4.4 \times 10^{-10} \cdot N_O}{d^2} \cdot x + \left(\frac{U_O}{d} + 4.4 \times 10^{-10} \cdot N_O \right)^2 \right]^{1/2}$$

Fig.A-2 shows a plot of E versus x.

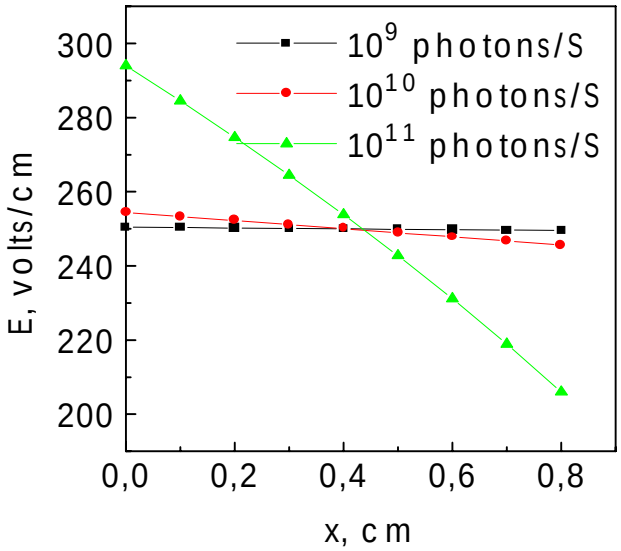

Fig.5.1-2. Net electric field intensity considering space charge effect and 200 V applied to electrodes.

From fig.A-2 it is evident that at lower intensities the perturbations due to space charge are negligibly small. However at higher intensities (>10^{10} photons/S) the effect is no more negligible and must be taken into account. Because of the accumulation of space charge, the electric field intensity is no more constant inside the active volume. This affects the drift of electrons. In region where the electric field is low, the parasitic electron capture probability and recombination losses increase and lead to loss of information. Since this effect is dependent on the incident photon intensity, therefore it the system is not properly designed, it can lead to non-linearity in the measurements. The effect can be minimized by keeping the electrode separation small and operating the system at high electric field. The use of high purity filling gas with an admixture which does not exhibit high electron capture cross section (Appendix-D), for example argon with methane, can also circumvent this problem.

APPENDIX-B

B.1. Drift and Diffusion in Gases

Both the electrons and ions produced as a result of passage of photons quickly lose their energy by multiple collisions with gas molecules. In the absence of externally applied electric field, the electrons and ions having energy E are characterized by the Maxwellian energy distribution [Sitar et al. 1993],

$$F(E) = C\sqrt{E}\,exp(-E/kT)$$

Where k is the Boltzmann's constant and T is the absolute temperatue.

In an external electric field is now applied, the electrons, because of their very small mass, experience a strong force and therefore do not generally retain their Maxwellian distribution. On the other hand, the distribution of ions is not affected if the applied electric field is not high enough to cause discharge in the gas [Sitar et al. 1993]. In the following we discuss briefly the movement of electrons and ions in the presence of externally applied field.

B.1.1. Motion of Electrons in an Electric Field

If a constant electric field is applied between the electrodes, the electrons, owing to their small mass, are rapidly accelerated between collisions and thus gain energy. The energy which these electrons lose through collision with gas molecules is not very large (again because of their small mass). Consequently the mean electron energy of electrons increases and the distribution is no longer Maxwellian.

Along the electric field lines, the electrons drift with velocity v_d which is usually an order of magnitude smaller than the velocity of thermal motion v_e.

However the magnitude of drift velocity depends on the applied electric field and finds its limits at the breakdown in the gas. The approximate dependence of drift velocity on the electric field E is given by [Rice-Evans 1974],

$$v_d = \frac{2eEl_{mt}}{3m_e\overline{v_e}}$$

Where l_{mt} is the mean momentum tranfer path of electrons.

Using theory of electron transport in gases, more precise expressions for drift velocity and other related parameters have been obtained and reported by many authors [Sitar et al, 1993].

Fig.B.1-1. shows the dependence of drift velocity on the applied electric field strength for different gases. It can be seen that in argon the drift velocity of electron is a very weak function of the electric field.

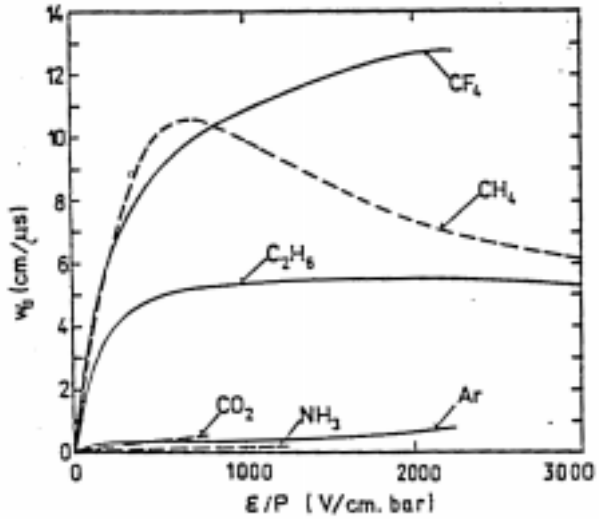

Fig.B.1-1. Electron drift velocities in different gases [Sitar et al. 1993]

Apart from motion due to drift field, the electrons diffuse in the gas due to thermal motion too. This motion is characterized by diffusion coefficient which is a scalar in the absence of electric field showing the isotropic nature of diffusion phenomenon. In the presence of externally applied electric field, however, the diffusion is no longer isotropic and the diffusion coefficient is a

tensor with two non-zero components D_L and D_T. For many gases, the longitudinal diffusion coefficient D_L is smaller than the transverse diffusion coefficient D_T [Sitar et al]. Table B.1-1 gives the diffusion coefficients for thermal electrons in the absence of electric field in noble gases.

Table B.1-1. Diffusion coefficients of electrons in noble gases in the absence of electric field [Allkofer 1969]

Gas	D, cm^2/s
He	310
Ne	3000
Ar	370
Xe	43

B.1.2. Motion of Ions in an Electric Field

Owing to the larger mass of ions, their thermal velocity is significantly lower than that of electrons. Furthermore the ions do not attain very large velocities in the presence of electric fields applied normally in radiation detectors. Because of this their distribution remains Maxwellian even in the presence of electric field. The drift velocity of ions depends linearly on the applied electric field and is given by,

$$v_+ = \mu_+ \frac{E}{P}$$

Here P is the pressure of gas and μ_+ is the mobility of ions in the gas. It is practically independent of E/P.

The drift velocity of ions is roughly three orders of magnitude lower than that of electrons. The slow movement of ions causes problems of space charge accumulation in the active volume of ionization detectors thus decreasing

the effective electric field strength. In section 5.1 the effect of space charge in the constructed beam monitor has been discussed quantitatively.

The diffusion coefficient of different ions in their own gases are given in table B.1.2-1.

Table B.1.2.-1. Diffusion coefficient and mobility of ions in their own gas under normal conditions [Sauli 1977]

Gas	D_+, cm^2/s	μ_+, $cm^2/(V.s)$
H_2	0.34	13.0
He	0.26	10.2
Ar	0.04	1.7
O_2	0.06	2.2
H_2O	0.02	0.7

The mobility of ions is a function of the type of ion and the gas in which it moves. Table B.1.2-2 gives the mobility of different positive ions in different gases.

Table B.1.2-2. Mobility of positive ions ($cm^2/(Vs)$) in different gases under normal conditions (experimental data) [Smirnov 1968; Elecki et al. 1975, Sauli 1977].

Gas	He^+	Ne^+	Ar^+	Kr^+	Xe^+	CO_2^+	CH_4^+
Same	10.2	4.1	1.7	0.94	0.58	1.09	2.26
He	10.2	24.0	19.5	20.2	18.0		
Ne	17.2	4.1					
Ar			1.7	2.3		1.72	1.87

The drift velocity of ions in gases is essentially linearly dependent on the externally applied electric field. This can be seen in fig.B.1.2-1 which shows the dependence of drift velocity on the reduced electric field E/P. The motion of ions in the active volume of the chamber is a very critical problem and must

be carefully examined. The space charge effect caused by accumulation of positive ions and subsequent reduction of effective electric field becomes significant at high incident photon rates. In Appendix-A the space charge effect and in Appendix-C the recombination losses in the active volume of the beam monitor have been investigated.

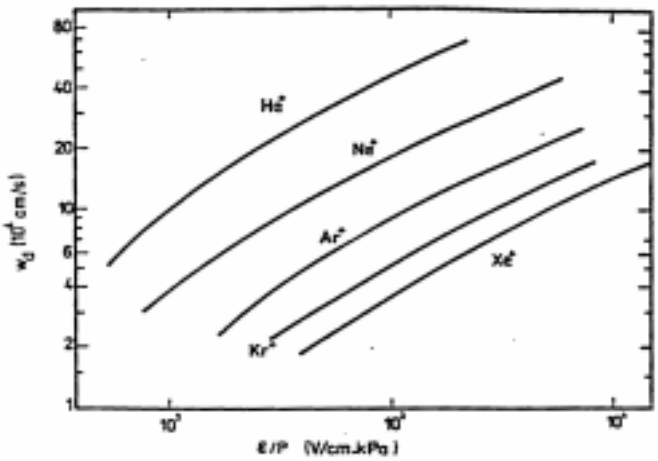

Fig.B.1.2-1. Drift velocities of positive ions in noble gases [McDaniel 1964]

APPENDIX-C

Recombination Losses

Ideally the measured ionization current in an ionization chamber should consist of all the electron-ion pairs generated in the active volume. However, due to different losses, the electrons and ions are not fully collected. For precision measurements, these losses must be taken into account. The recombination of electrons and ions is one of the major source of uncertainty in measurements especially at high fluxes of incident photons. Intuitively one can think that the recombination rate should depend directly on the concentration of charges. This suggests that the rate of change in the number of positive and negative charges should be proportional to the number of charges themselves, i.e.,

$$\frac{dn^+}{dt} = S - \alpha \cdot n^+ \cdot n^- \qquad \text{(C-1a)}$$

$$\frac{dn^-}{dt} = S - \alpha \cdot n^+ \cdot n^- \qquad \text{(C-1b)}$$

Here α is the recombination constant and S represents the source of charges.

The above two equations imply,

$$\frac{d(n^- - n^+)}{dt} = 0$$

or

$$n^- = n^+ + C_1 \qquad \text{(C-2)}$$

C_1 is the integration constant and it's value depends on the initial difference of positive and negative charges.

Substitution of (C-2) in (C-1b) gives,

$$\frac{dn^-}{dt} = S - \alpha \cdot (n^-)^2 + \alpha \cdot C_1 \cdot n^- \qquad \text{(C-3)}$$

The solution to this differential equation is,

$$n^{-} = \frac{r_1 - r_2 \cdot C_2 \cdot exp\left(\sqrt{C_1^2 + 4 \cdot S/\alpha} \cdot t\right)}{1 - C_2 \cdot exp\left(\sqrt{C_1^2 + 4 \cdot S/\alpha} \cdot t\right)} \qquad \text{(C - 4)}$$

where r_1 and r_2 are the roots of the quadratic equation on right hand side of (C-3), given by

$$r_1, r_2 = \frac{1}{2}\left[C_1 \pm \sqrt{C_1^2 + 4 \cdot S/\alpha}\right]$$

The solution for positive charges is also given by (C-4) but in this case the roots are given by,

$$r_1, r_2 = \frac{1}{2}\left[-C_1 \pm \sqrt{C_1^2 + 4 \cdot S/\alpha}\right]$$

The values of the constants C_1 and C_2 can be determined by using the boundary conditions $n=n_0$ at $t=0$ and $n=n$ at $t=t$.

Equation (C-4) implies that the concentration of positive or negative charges increase as a complex transcendental curve and approach the steady state value of

$$n_\infty = r_2$$

as t becomes very large.

For a special case when the initial concentrations of positive and negative charges are equal, the constant C_1 assumes the value zero according to (C-2) and the steady state charge concentration becomes,

$$n_\infty = \sqrt{S/\alpha}$$

Hence the equilibrium or steady state charge concentration is completely determined by the source producing electron-ion pairs and the recombination coefficient.

The numerical value of the recombination coefficient has been reported by different authors. The data is unfortunately contradicting and points to the fact that the measurement of the parameter is not easy. In order to get a quantitative idea of the recombination process in the constructed beam monitor, a value of 10^{-6} cm^3/ion-sec has been taken from [Biondi, 1953]. The value does not represent the experimental situation here because the parameter was measured by Biondi at a pressure of 20-30 mmHg. In any case the value should give us at least an estimate of the involved quantities.

This steady state value of charge density inside the active volume of the chamber determines the ionization current which flows as a result of applied electric field. From the above relation one can get an estimate of the number of charge carriers in steady state condition. Fig.C-1 shows the quadratic dependence of steady state charge density on the number of absorbed photons in the constructed beam monitor. Here it has been assumed that the incident 10keV photon beam has an area of 4X8 mm^2 and the filling gas in the chamber is argon.

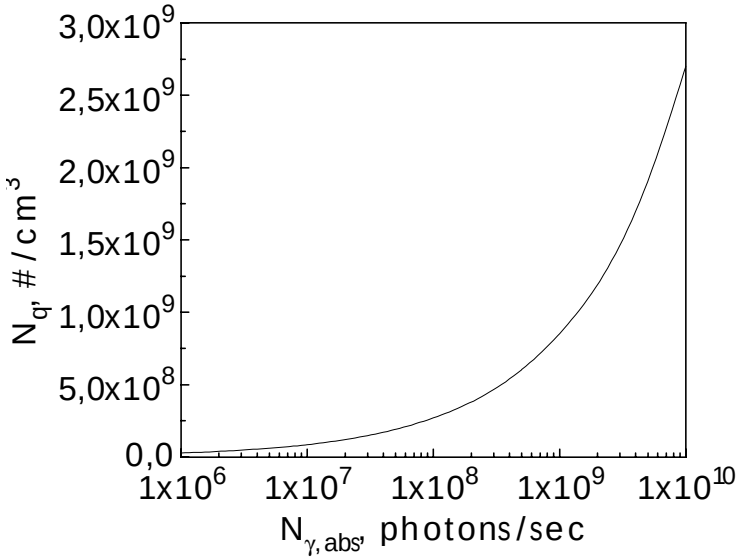

Fig.C-1. Dependence of steady state charge density on the number of absorbed photons.

It is evident that the steady state charge density does not depend linearly on the number of absorbed photons. But as stated earlier these values do not in

any way depict the actual situation of the beam monitor because we have taken a value of recombination coefficient which does not represent our experimental set up.

Furthermore, by the application of the electric field, the ions and electrons experience a force which moves them towards respective electrodes, hence reducing the recombination probability. We have however not taken into account the effect of electric field in our calculation of recombination losses. We have seen in the data analysis of the experiments done with the beam monitor that the system behaves very linearly with respect to incident photon flux which means that the above mentioned non-linearity is not present in the system.

APPENDIX-D

Effects of Contamination in the Detector

The capture of electrons by electronegative impurities in the active volume of the chamber leads to the loss of ionization information. The probability of attachment in gases having high electron affinities is high because such atoms form stable negative ions. Table D-1 shows the electron affinities of different molecules and ions normally found in ionization chambers either as admixtures or as impurities.

Table D-1. Electron affinity of different ions and molecules [Kondratev, 1974]

Molecular ion	Electron affinity, eV	Negative ion	Electron affinity, eV
O_2	0.44	O^-	1.467
C_2	3.54	C^-	1.27
Cl_2	2.38	Cl^-	3.614
OH^-	1.83	H^-	0.754

The capture of electrons can take place by various mechanisms,

Radiative Capture

In this mechanism the electron is captured by an atom which goes into an unstable higher excited state. The atom stabilizes itself by emitting a photon.

$$e^- + Z \rightarrow Z^- + h\nu \qquad \text{(D-1)}$$

This process occurs when the atom exhibits positive electron affinity. The cross-section for radiative capture is not very large for atomic species of interest in radiation detectors [Sitar et al., 1993].

Electron attachment involving three body collisions

In this process the excess energy is transferred to a third body (another atom or electron).

$$e^- + Z + X \rightarrow Z^- + X + energy$$
$$e^- + e^- + Z \rightarrow Z^- + e^- + energy \qquad \text{(D - 2)}$$

Electron attachment to a molecule without dissociation

The excess energy in this process is transferred to a third body.

$$e^- + YZ \rightarrow (YZ)^{-*} \quad , \quad (YZ)^{-*} + X \rightarrow (YZ)^- + X + energy \qquad \text{(D - 3)}$$

The cross section of this process is large and it exhibits resonant character if the atom X (usually termed as catalyst) is capable of taking over all the energy generated in the capture [Sitar et al., 1993].

Dissociative capture

The dissociative capture process takes place in molecules which exhibit small dissociation thresholds. It can occur in a number of ways,

$$e^-(E_e) + (XY...VZ) \rightarrow (XY...VZ)^{-*} \rightarrow$$
$$\rightarrow (XY...VZ)^* + e(E_e' < E_e) \; ; \qquad \text{(D - 4a)}$$
$$\rightarrow \left.\begin{matrix} XY^* + VZ^- \\ (XY...V)^* + Z^- \end{matrix}\right\} ; \qquad \text{(D - 4b)}$$
$$\rightarrow (XY)^* + VZ^{-*} \left.\begin{matrix} \rightarrow VZ^* + e^- \\ \rightarrow V^* + Z^- \end{matrix}\right\} ; \qquad \text{(D - 4c)}$$
$$\rightarrow (XY...VZ)^- + energy \; ; \qquad \text{(D - 4d)}$$

Mechanism (a) is the inelastic collision in which the incident electron losses only a part of its energy; (b) represents the dissociative capture of an electron

involving the production of stable negative ions; in (c) the dissociative capture of an electron is followed by the creation of metastable negative ions; (d) represents the formation of negative ions.

Although the attachment cross sections for thermal electrons in oxygen and water are not very high (due to the high thresholds for molecular dissociation, see e.g. [Sitar et al., 1993]), they are the principal gas contaminants in ionization chambers. In the case of large electron drift length (of the order of a cm) their influence on collection of charge is significant. Normally several parts per million of oxygen are present in chambers and its concentration increases due to diffusion through the mylar windows of the chamber and to degassing of the other parts inside the chamber. The amount of water vapors is a gas mixture is even greater.

The capture of electrons is enhanced if gases such as CO_2 or isobutane are present in the gas mixture. These gases act as catalysts for the reaction represented by (D-2) and (D-3). The electron capture rate in mixtures containing methane has been found to be lowest [Sitar et al., 1993]. This means that the mixture of argon and methane is preferable as compared to that of argon and carbon dioxide as the filling gas for the beam monitor.

The degradation of performance when using argon and carbon dioxide mixture was observed during experiments with the beam monitor. The ionization chamber plateaus obtained for this gas mixture had variations of more than 3% per 1000 volts. This was decreased to less than 2% per 1000 volts when this gas mixture was replaced by argon and methane. The higher electron capture property is responsible for capture of more electrons at lower applied electric field. As the voltage applied to the chamber is increased, the electrons experience stronger force and are less susceptible to the capture by CO_2 molecules and consequently the ionization current increases.

Mathematically the electron attachment is characterized by the probability of capture in a single collision [Sauli 1977],

$$k_a = l_e < \sigma_{at} > n_a = \frac{1}{< \tau_{at} > \nu_e} \qquad \text{(D-1)}$$

Here $<\sigma_{at}>$ is the mean capture cross section and $<\tau_{at}>$ is the mean lifetime of electrons before capture. Table D-2 shows these quantities for some gases usually found in ionization chambers either as admixture or as impurity.

Table D-2. Capture probability, mean capture time and collision frequency of thermal electrons under normal conditions [Sauli 1977]

Gas	k_a	$<\tau_{at}>$, s	ν_e, s^{-1}
O_2	6.2×10^{-9}	7.1×10^{-4}	2.2×10^{11}
CO_2	2.5×10^{-5}	1.9×10^{-7}	2.1×10^{11}
H_2O	2.5×10^{-5}	1.4×10^{-7}	2.8×10^{11}
Cl_2	4.8×10^{-4}	4.7×10^{-9}	4.5×10^{11}

It can be seen that in oxygen or water the electrons are very quickly captured (within several hundreds of a nanosecond). Therefore even small amounts of these gases can deteriorate the signal to unacceptable levels. Care must be taken to ensure that the volume concentration of these impurities in the active volume of the chamber is as low as possible. The mean capture time in carbon dioxide is, however, a fraction of a millisecond. But since this gas is normally used in large quantities (as admixture) in the detectors, therefore its overall effect is deteriorating and can not be neglected.

In view of these considerations, it can be said that a mixture of argon and methane is preferable over argon and carbon dioxide as filling gas in the beam monitor.

References

[1] Ahmed, S. N. et al, A High Precision Beam Intensity Monitor for Synchrotron Radiation Experiments, in preperation.

[2] Allkofer O. C, 1969, Spark Chambers, Thiemig, München.

[3] Baj B., 1993, Entwicklung und Bau einer Vielkanal-Ionisationskammer zurStrahlüberwachung für die Digitale Substraktionsangiographie, Diplomarbeit, Uni.-GH-Siegen.

[4] Biondi, M.A. and S.C. Brown, 1953, Phys. Rev. 90, 730.

[5] Browne E. and Firestone R. B., 1986, Table of Radioactive Isotopes, John Wiley & Sons, New York.

[6] Claus Grupen, 1996, Particle Detectors, Cambridge University Press, 1996.

[7] Delaney C. F. G., Finch E. C., 1984, Some Simple Considerations on Pulse Shape in Radiation Detectors, Am. J. Physics, Vol. 52, No. 4.

[8] Elecki A. V. et al., 1975, Transport Phenomena in a Weakly Ionized Plasma, Atomizdat, Moscow.

[9] Goulon J., 1991, Detectors Optimized for X-Ray Absorption Spectroscopy, Proc. Of the European Workshop on X-Ray Detectors for Synchrotron Radiation Sources, France.

[10] Kondratev V.N. (Ed.), 1974, Energies of Chemical Bonds, Ionization Potentials, Electron Affinities, Moscow.

[11] Leo W. R., 1994, Techniques for Nuclear and Particle Physics Experiments, Springer-Verlag.

[12] Lyons Louis, 1992, Statistics for Nuclear and Particle Physicists, Cambridge Univ. Press, Cambridge.

[13] Margaritondo Giorgio, 1988, Introduction to Synchrotron Radiation, Oxford Univ. Press, New York.

[14] McDaniel E. W., 1964, Collision Phenomena in Ionized Gases, Wiley, New York.

[15] Menk, R.-H, 1994, Eine Vielkanalionisationskammer für Röntgenbildaufnahmen, Diss., Uni.-GH-Siegen.

[16] Myalistin V. K. et al, 1992, A Multichannel Position Sensitive Ionization Chamber for X-ray Intensity Monitoring, Nucl. Instr. Meth., A323 97-103.

[17] Myalistin V. K. et al, 1991, Position sensitive Monitor Chamber at the Limit of Quantum Noise, Proc. of the European Workshop on X-ray Detectors for Synchrotron Radiation Sources, France.

[18] Necula A. et al, 1993, An Experimental Study of the Statistical Fluctuations of an Ionization Chamber Current, Nucl. Instr. Meth. A332 501-505.

[19] Rice-Evans P., 1974, Spark, Streamer, Proportional and Drift Chambers, Richelieu, London.

[20] Sauli F., 1977, Prep. CERN 77-09.

[21] Schenk, H. W., 1991, Optimierung eines Bildgebenden Röntgendetektors im Bereich des Quantenrauschens, Diss., Uni.-GH-Siegen.

[22] Sitar B. et al., 1993, Ionization Measurements in High Energy Physics, Springer-Verlag.

[23] Smirnov B. M., 1968, Atomic Collisions and Elementary Processes in Plasma, Atomizdat, Moscow.

[24] Veigele WM. J., 1973, Photon Cross Sections from 0.1keV to 1MeV for Elements Z=1 to Z=94, Atomic Data Tables, 5, 51-111.

[25] Walenta A. H., Besch H.-J., 1994, Gas-filled Detectors in Medical and Industrial Imaging, Proc. SPIE, X-ray and UV Detectors, Vol. 2278, California.

Acknowledgements

In the Name of Allah, The Benificient, The Merciful.

My wife (Rahat) and children (Hiba and Shozab) deserve special thanks and acknowledgements for their understanding, patience and help throughout the project. The continuous encouragement and moral support I received from my parents and other family members was the driving force specially during the hard times of the project.

Special thanks are due to Prof. A. H. Walenta for supervising the project in a very professional and experienced way. I thank Dr. H.-J. Besch for his continuous help in technical matters without which the project would not have been successfully completed. Thanks are also due to Prof. N. Pavel whose valuable suggestions in the last stages of the project and during thesis writing were more than helpful.

I thank Mr. G. Iksal who developed a part of electronics chain of the beam monitor and whose technical suggestions on a number of difficult electronics design and application stages were very helpful. Thanks are also due to the mechanical workshop of Siegen University for building the mechanics of the monitor. I also thank Dr. W. Schenk for his valuable suggestions at the start of the project.

In the end I thank all our group members who provided a very friendly and helpful working environment.